NASA CR-127488

IN-FLIGHT COMPARISONS OF BOUNDARY-LAYER AND WAKE MEASUREMENT PROBES FOR INCOMPRESSIBLE FLOW

Lawrence J. Mertaugh, Jr.

Mississippi State University
Department of Aerophysics and Aerospace Engineering
State College, Miss.

March 1972

Prepared for

NATIONAL AERONAUTICS AND SPACE ADMINISTRATION
Washington, D.C. 20546

1. Report No.	2. Government Accession No.	3. Recipient's Catalog No.
NASA CR-127488		

4. Title and Subtitle	5. Report Date
In-Flight Comparisons of Boundary-Layer and Wake Measurement Probes for Incompressible Flow	March 1972
	6. Performing Organization Code

7. Author(s)	8. Performing Organization Report No.
Lawrence J. Mertaugh, Jr.	AASE Report No. 72-74
	10. Work Unit No. 136-13-01-00-24
9. Performing Organization Name and Address Mississippi State University Department of Aerophysics and Aerospace Engineering State College, Mississippi	11. Contract or Grant No. NGR-25-001-036
	13. Type of Report and Period Covered Contractor Report
12. Sponsoring Agency Name and Address National Aeronautics and Space Administration Washington, D. C. 20546	14. Sponsoring Agency Code

15. Supplementary Notes

16. Abstract

This report presents the results of in-flight comparisons of a number of boundary-layer and wake measurement probes suitable for low-speed flight-test investigations. The tested boundary-layer probes included a traversing total-pressure probe and a hot-film probe mounted on an internally-mounted drive mechanism, a curved and a straight boundary-layer rake, and a traversing hot-film probe with an externally-mounted drive mechanism. The wake measuring devices included a traversing, self-aligning probe, a wake rake, and an integrating wake rate. The boundary-layer data are compared with a common reference velocity profile and comments given regarding the accuracy of the static-pressure and total-pressure measurements. Discussions on the various calibration presentations used with hot-wire and hot-film sensors and various aspects of improving the accuracy of hot-film sensor results are given in the appendix of this report.

17. Key Words (Suggested by Author(s))	18. Distribution Statement
In-flight boundary-layer measurement techniques Boundary-layer probes Boundary-layer sensors	Unclassified - Unlimited

19. Security Classif. (of this report)	20. Security Classif. (of this page)	21. No. of Pages	22. Price*
Unclassified	Unclassified	71	

*For sale by the Clearinghouse for Federal Scientific and Technical Information
Springfield, Virginia 22151

TABLE OF CONTENTS

IN-FLIGHT COMPARISONS OF BOUNDARY-LAYER AND WAKE MEASUREMENT PROBES FOR INCOMPRESSIBLE FLOW

By Lawrence J. Mertaugh, Jr.
The Department of Aerophysics and Aerospace Engineering
Mississippi State University

INTRODUCTION

Vertical arrays of total-pressure probes, boundary-layer rakes, or mice, wake rakes, and traversing, total-pressure probes or hot-wire probes have been used for many years to measure the velocity and momentum distribution within boundary layers and wakes of aerodynamic surfaces. In general, these measurements are made in wind-tunnel facilities with very limited data obtained on actual flight vehicles. Although the advantages of the closely controlled test conditions normally found in the wind tunnel are well known, the difficulty in duplicating the low level of free-stream microscale turbulence, the full-scale Reynolds number, and the free-stream boundary conditions often detract from the validity of the wind-tunnel data. Measurements made on an actual flight vehicle are obviously desirable for at least certain types of test programs.

While the use of these measurement devices in the wind tunnel is well documented, with some information available regarding flight-test utilization, there are only limited data available on the relative capabilities of these devices. References 1, 2, and 3 present some comparative test data between traversing pitot tubes and various boundary-layer rake configurations, and reference 4 gives a comparison between a traversing, wake probe and an integrating, wake rake. These are the only references found in an extensive literature search on the subject of boundary-layer and wake measurements that provide comparative test data. Although these reports undoubtedly satisfy the respective authors objectives, they do not provide an extensive source of material for evaluating the relative merits of the various measurement devices.

In the case of hot-wire (or hot-film) probes, no data comparing the hot-wire results with suitable pneumatic measurements are found in the literature except for the basic calibration data. The calibration data do constitute comparisons in the environment of the calibration equipment, but these data do not always represent a true comparison in the test environment. The significant aspect of most of the experimental uses of hot-wire equipment is that measurements are obtained essentially under the same ambient conditions as the calibration. Many authors claim to have the proper choice of test parameters to allow the extension of the calibration data to other test conditions, but the actual use of these methods, showing comparative and repetitive measurements, is not found in the literature. This is an important consideration for flight-test work because of the large range of test conditions that are normally encountered in flight.

The objective of the test program discussed in this report is to provide in-flight comparisons of boundary-layer velocity and wake drag measurements using a number of measurement devices. Discussions of some of the problems and limitations imposed by the variations in test environment and the less closely controlled test conditions associated with flight-test studies are also included. Only the mean velocity measurements in the boundary layer and wake were considered in this program. This work represents the second phase of a program to review, catalog, and where possible, evaluate the various measurement devices that lend themselves to the measurement of boundary layers and wakes on low-speed flight-test vehicles. The results of the literature search and consequent cataloging of the equipment suitable for flight test are found in reference 5.

The comparative tests were conducted on a glove section built onto the wing of a TG-3 glider. The wing planform and the lack of a propeller provided essentially two-dimensional flow over the glove section. The test position was located in an adverse, chordwise, pressure gradient, and a consistent turbulent boundary layer was ensured by the use of a trip wire. Boundary-layer measurements were obtained from two boundary-layer rakes, an externally mounted, traversing, hot-film probe, and an internally mounted, traversing probe holder that supported a total-pressure probe and a hot-film probe. The wake measurements were with a traversing, self-aligning, pitot-static probe, a wake rake, and an integrating, wake rake.

All test data were obtained at a single equivalent flight speed of 91.4 miles per hour (local velocity at the test section of 160 feet per second) and with test altitudes extending from 1,000 feet to 10,000 feet.

SYMBOLS

A, B and C	constants
BTU	British thermal unit
C_d	two-dimensional drag coefficient, $\frac{D}{c\rho_{std}u_e^2/2}$
C_f	skin friction coefficient, $\frac{\tau_w}{p_{std}u_e^2/2}$
C_p	pressure coefficient, $\frac{p-p'}{\rho_{std}u_e^2/2}$
c	airfoil section chord, feet or inches

c_p	specific heat at constant pressure, BTU/slug-^oF
D	drag force, pounds
d	hot-film sensor diameter, feet or inches
E_b	anemometer bridge voltage (after volt drop), volts
E_{b_o}	anemometer bridge voltage (after volt drop), with zero velocity over sensor, volts
H_{12}	boundary-layer shape parameter, δ_1/δ_2
h	surface coefficient of heat transfer, BTU/hour-foot^2-^oF
K	constant
N_{Gr}	Grashof number, $gd^3\beta\ \theta/\nu^2$
N_{Kn}	Knudsen number, λ/d
N_{Nu}	Nusselt number, hd/κ
N_{Pr}	Prandtl number, $\nu\rho\ c_p/\kappa$
N_{Re}	Reynolds number, $\rho u_t d/\mu$
$N_{Re(\delta_2)}$	Reynolds number, $\rho u_t \delta_2/\mu$
p	pressure, pounds/foot^2
p'	free-stream pressure, pounds/foot^2
R	resistance of probe and lead, ohms
R_o	operating resistance of probe and lead, ohms
R_1	resistance of probe and lead at 25^{o}C, ohms
s	surface distance, feet or inches
T	temperature, ^oC or ^oK

T.E.	trailing edge of glove section
u	velocity, feet/second
$\bar{u}$	statistical mean velocity, feet/second
u_e	equivalent velocity, for this speed regime
	$u_e \simeq ((p_t-p)2/\rho_{std})^{0.5}$, feet/second
W	sensor electrical power, watts
y	distance normal to the surface, feet or inches
α	temperature coefficient of resistivity, $1/^oC$
β	cubic coefficient of thermal expansion, $1/^oK$ (assume $\beta=1/T$)
δ	boundary-layer thickness, feet or inches
δ_1	boundary-layer displacement thickness, $\int_o^\infty (1-\frac{u}{u_\infty})$ dy, feet or inches
δ_2	boundary-layer momentum thickness, $\int_o^{\infty-u} \frac{}{u_\infty} (1-\frac{u}{u_\infty})$ dy, feet or inches
θ	temperature excess, ^oK
κ	thermal conductivity, BTU/hour-foot-^oF
λ	molecular mean free path, feet or inches
μ	absolute viscosity, slug/feet-second
ν	kinematic viscosity, $feet^2$/second
Π	constant
ρ	density, $slug/foot^3$
τ	shear stress, $pounds/foot^2$

Subscripts:

f	film
g	gas ("ambient" conditions at the test position)
o	ambient conditions at altitude
std	standard sea-level conditions
t	true or stagnation conditions (total)
w	sensor surface
25	based on $25^{\circ}C$
∞	outside the boundary layer ($y = \infty$)

TEST PHILOSOPHY AND PROCEDURE

The selection of the test instrumentation and the procedure followed in the test flights was an attempt to minimize the influence of pilot technique and measurement system errors on the evaluation of the relative merits of the test probes. Although this objective was not completely realized due to problems with equipment and the very nature of flight testing (discussions of these aspects of the program are provided in later sections of this report), the final results are considered to be illustrative of the difficulties associated primarily with the probe configuration rather than the measurement system. This statement is true for the tests of the hot-film probes only if the electronic equipment associated with the operation of the hot-film probe is considered a part of the probe system rather than the measurement system.

The measurement system used in this program consisted of a single, differential-pressure transducer, in conjunction with a Scanivalve, and a manually-read, digital voltmeter. The digital voltmeter provided the most accurate form of readout available at this facility during the time period of this test program. While manually acquiring the test data was an obviously slow process, it did allow the observer to screen the readings and to neglect non-steady values due to flight velocity changes or atmospheric turbulence. This slow reading rate also tended to make the individual data points more statistically independent which minimized consistent or progressive bias in a given set of data points. The limited, statistical evaluation of the accuracy of the test data is more realistic because of this independence. The use of a single pressure transducer for all pressure measurements was intended to eliminate the effect of transducer differences on the probe evaluation.

The test flights were normally conducted soon after sunrise to reduce exposure to atmospheric turbulence and to allow testing at more moderate temperatures. The test equipment was turned on, checked and given an initial adjustment prior to takeoff. The tow to altitudes, normally 10,000 feet, required about 15 minutes and provided adequate time for the transducer box temperature to stablize and for the electronic equipment to warm up. Final adjustments and check readings were accomplished just prior to glider release. Ambient temperature readings were normally taken at 1,000-foot altitude intervals during the tow. Testing was started when a stabilized airspeed was established after release. Data recording was interrupted when any deviations from the desired, straight, stabilized flight path were noted by either the pilot or the observer. Test temperatures and pressures were recorded periodically during the data runs for the hot-film probe. Ground readings and equipment adjustment checks were obtained prior to leaving the runway area after landing.

TEST EQUIPMENT

TG-3 Glider

The test vehicle, shown in figure 1, was a two-place glider with a glove section installed on the inboard, untapered portion of the left wing. The glove section was constructed of glass reinforced polyester resin and consisted of 24 layers of glass cloth laid directly over the wing (NACA-4416) airfoil section. The plastic surface extended from the wing trailing edge forward over the upper surface and back to the wing spar on the lower surface. The thickness of the lower surface was tapered, starting at the leading edge, so as to fair into the existing section lines at the spar. The upper surface skin thickness was approximately 0.27 inch and with the basic wing structure provided adequate rigidity to preclude surface distortions during the test program. The glove fabrication technique resulted in a rather blunt trailing edge with an effective radius of approximately 0.25 inch. An aluminum access panel was provided in the lower surface of the glove. The edges of the access panel were sealed with plastic tape for the test flights.

The dimensional layout of the glove is shown in figure 2. The test position was located at approximately 66 percent of the chord. Two partial chordwise rows of static-pressure taps, 14 taps in each row, were provided 11.25 inches on either side of the test position. Two additional static-pressure taps were located 1.0 inch to each side and at the same chordwise location as the test position. One permanent, total-pressure tube was mounted 6.09 inches inboard of the test position and 1.0 inch above the surface. A boundary-layer trip wire, 0.02 inch in diameter, was mounted at approximately 25 percent of the chord.

The TG-3 glider weight and center of gravity were controlled by means of ballast mounted in the nose and at the observer's station. The ballast was adjusted for changes in instrumentation and aircraft equipment. The nominal gross weight was 1580 pounds with the center of gravity located 18 inches aft of the basic wing leading edge.

Instrumentation

A sensitive, helicopter airspeed indicator and a standard altimeter were used for the flight instruments. A Kiel tube, mounted on the nose of the glider, and a self-aligning, static-pressure probe, mounted on the top of the vertical tail, were used as pressure sources for the flight instruments. The flight instrument system was balanced and a panel vibrator was used on the pilot's instrument panel. Two standard outside-air-temperature gages, mounted on each side of the pilot's canopy, were used to measure ambient temperature.

All electrical output from the pressure transducer, position transducer, and hot-film anemometer was hand recorded by the test observer using a digital voltmeter. The voltmeter was of the integrating type, powered from internal batteries, and provided with an internal 10-volt reference. The voltmeter was operated on the plus-or-minus 10.0-volt range and the zero and full-scale adjustments were checked at the beginning and end of each data run. Changes in the indicated zero and full-scale readings, over the duration of the test flight, were seldom in excess of 0.01 volt which was the minimum significant reading on the meter display. The pressure transducer was connected to the various pressure sources through a Scanivalve. Free-stream total pressure was used as the reference pressure for the differential, variable-reluctance, self-contained, DC-to-DC pressure transducer. The transducer box temperature was maintained between 75 and 85°F. The transducer was powered from the forward 24-volt batteries.

The anemometer was a commercially available, constant-temperature unit operating from the rear 24-volt batteries. It should be noted that, as used in this report, the word anemometer denotes the electronics module (i.e. the power supply, bridge circuit, feedback amplifier, and operating controls) associated with the operation of the hot-film sensor. The operating resistance of the unit was set by means of a plug-in, fixed resistor. A voltage divider was used to keep the output voltage within the 10.0-volt range of the voltmeter. The output-to-input ratio of the divider was 0.535.

A schematic diagram showing the electrical layout of the instrumentation system is given in figure 3.

Internal, traversing probe holder and total-pressure probe. - The internal, traversing probe holder, shown in figure 4, utilized a screw drive powered by an in-line, geared, fractional-horsepower, 28-volt DC motor operated from 24-volt aircraft batteries. Although the rating of the motor was unknown, the stall current was 1.0 amp at 28 volts. Position data were obtained from a linear potentiometer. The potentiometer excitation voltage, as well as the output voltage, was measured in flight to compensate for variation in battery voltage. Limit switches were provided which gave a total available travel of 0.9 inch. Probe height adjustment was accomplished by changing the position of the probe-holder shaft in the drive-screw-follower block. Although provisions were made for routing the total-pressure or hot-film leads through the 0.125-inch, probe-holder shaft, external routing of these lines was used in these tests. The upper surface of the holder frame was secured to the inner surface of the glove skin for these tests.

The total-pressure probe was permanently secured to the probe holder for the tests. The probe was constructed from 0.050-inch (outside diameter) stainless steel tubing (0.034-inch inside diameter) with the forward end flattened and machined to give a height of 0.016 inch and a width of 0.066 inch. The internal height of the probe opening was 0.006 inch. The general configuration of the probe may be seen in figures 4 and 5. Figure 5 also shows the external routing of the hot-film and total-pressure leads used in these tests.

External, traversing probe holder. - The external, traversing probe holder is shown mounted on the glove surface in figure 6. This probe was originally designed for boundary-layer measurements on the wing of an aircraft equipped with a suction boundary-layer-control system. The design objectives were to provide a device which would give a minimum obstruction within the boundary layer, would obscure a minimum number of suction holes on the wing of the aircraft, and would have a probe travel of at least 1.0 inch. The basic design incorporated various combinations of probe-holder leg lengths and probe-holder arm shapes to allow measurements on the flattened surfaces found toward the rear of most airfoils and on the leading edge of highly cambered airfoils. The legs were airfoil shaped, in cross-section, and were taped to the surface of the glove for these tests. The probe movement, towards the glove surface, was controlled by a fouling strip glued to the glove surface and the fouling wire mounted on the probe. Contact between the wire and the strip stopped the probe drive motor. As used for these tests, the probe travel was approximately 0.9 inch. The probe arm was positioned with the ramp block which was moved by the lead screw, which was driven by the rear-mounted, 28-volt DC motor (figure 7). The aft end of the probe arm was held in contact with the ramp block by means of a leaf spring. Probe position data were obtained by means of a microswitch and multi-lobed cam, attached to the end of the lead screw, and a counter.

Hot-film probe. - The sensor of the hot-film probe consisted of a 0.006-inch, platinum film, quartz-coated rod with an active length of 0.08 inch. The sensor was commercially available and was mounted to the support arms of the probe by a local technician. The distance between the support arms was 0.10 inch with the overall rod length of approximately 0.125 inch. The sensor was secured to the support arms with soft solder. The sensors used in this program were relatively large but were selected for their mechanical strength and the fact that they could be replaced locally when broken. The next smaller-sized available sensor was 0.002 inch in diameter and required that the probe be returned to the factory for sensor replacement. The resulting probe was ideal for the present program since the non-steady characteristics of the boundary layer were not being studied. The advertised frequency response of the 0.006-inch film sensor, at a velocity of 300 feet per second, was 15,000 Hz.

The probe arms were of the 90°-bend type and, as can be seen in figures 4 and 5, included a fouling wire which was used with the external, traversing probe holder to limit the probe travel into the glove surface. The advertised, maximum operating temperature of the probe sensor was $500^{\circ}C$ with the recommended value for air being $275^{\circ}C$. A number of operating temperatures were used during this program, but the best results were obtained using

an upper limit of 300°C. The commercially-available, probe-holder socket was used with the external, traversing probe holder; slip-on electrical leads were used with the internal, traversing probe holder.

Curved, boundary-layer rake. - The curved, boundary-layer rake provided 16 total-pressure tubes and 1 static-pressure tube. Figure 8 shows a close-up view of this device. Each tube consisted of a 0.042-inch-outside- and 0.027-inch-inside-diameter, stainless steel tube soldered into and extending 0.5 inch forward of a 0.065-inch outside- and 0.047-inch inside-diameter, stainless steel tube. The forward 0.1 inch of each total-pressure tube was flattened to a height of 0.023 inch and a width of 0.052 inch. The internal height of the flattened opening of the tube was 0.006 inch. The static-pressure tube used four, 0.015-inch diameter holes located 5.2 tube diameters aft of the tube leading edge. The static taps were in the plane of the leading edges of the total-pressure tubes. The pneumatic connections between the rake and the Scanivalve were made with plastic strip tubing. The probe was secured to the glove with tape. Figure 9 shows the installation of the curved, boundary-layer rake on the glove surface.

Straight, boundary-layer rake. - The straight, boundary-layer rake provided ten, total-pressure tubes and one, static-pressure tube. A close-up view of this rake is shown in figure 10. Construction of this rake was similar to the curved rake except that only the lower seven, total-pressure tubes were flattened. The static-pressure taps were located 12.0 tube diameters aft of the rounded leading edge of the static-pressure tube on this rake. Plastic strip tubing was used to connect the pressure tubes to the Scanivalve. The installation of this rake on the glove surface is shown in figure 11.

Integrating, wake rake. - The integrating, wake rake, shown in figure 12, consisted of 27 total-pressure tubes which were soft soldered into a 0.5-inch diameter, thin-wall, manifold tube. The total-pressure tubes extended 7.6 manifold tube diameters (3.8 inches) forward of the manifold tube and had an outside diameter of 0.125 inch with an inside diameter of 0.075 inch. The outer, forward 0.1 inch of the total-pressure tubes was tapered to the tube inside diameter at the tube leading edge. The spacing of the total-pressure tubes was nominally 0.5 inch. The integrated total pressure was taken from the top of the manifold tube. The rake was mounted to the traversing, wake boom.

Wake rake. - The installation of the wake rake is shown in figure 13. The wake rake consisted of 21 total-pressure tubes and 3 static-pressure tubes mounted in a flattened piece of thin-wall tubing. The total-and static-pressure tubes were 0.065-inch-outside- and 0.047-inch-inside-diameter stainless steel tubing. The static taps were located in the plane of the leading edges of the total-pressure tubes and 7.7 tube diameters aft of the leading edges of the static-pressure tubes. The leading edges of the total-pressure tubes were squared off. The symmetrical vertical tube spacing, starting with the middle tube of the rake, was 0.25 inch for the first four tubes, 0.40 inch for the next tube, 0.60 inch for the next tube, and 1.00 inch for the remaining four total-pressure tubes. The total pressure tubes extended 15.2 support tube widths (3.80 inches) forward of the supporting tube. The

static-pressure tubes were in a plane 0.40 inch inboard of the plane of the total-pressure tubes and at the same vertical location as the first, seventh and eleventh total-pressure tubes, starting at the top of the rake. The wake rake was attached to the traversing, wake boom; pneumatic connections with the Scanivalve were made with strip tubing.

Self-aligning, traversing, wake probe and boom. - The self-aligning, wake probe utilized a pitot-static head connected, through a spherical bearing, to the supporting tube and, in turn, to the traversing, wake boom. The wake probe and boom are shown in figure 14. The total- and static-pressure lines were routed through the center of the spherical bearing, and stops were provided to prevent the self-aligning head from rotating about the longitudinal axis. Eight static-pressure taps were provided on the probe. These taps were located three tube diameters aft of the spherical nose of the probe. The static-pressure taps were 2.3 tube diameters forward of the fin-support leading edges. The probe tube diameter was 0.438 inch. The probe head was free to rotate about the lateral and directional axes approximately 30 degrees with respect to the longitudinal axis.

The traversing, wake boom was mounted to the fuselage structure and was rotated by means of a linear actuator which was powered by a 28-volt, DC motor. Limit switches were provided which, with the probe mounted at the spanwise station of the test position, gave a total probe travel of 10.0 inches. The distance from the probe to the axis of rotation of the traversing boom was 48.5 inches. Probe position data were provided by a microswitch and cam, mounted on the drive motor, and a counter.

CALIBRATION

All basic aircraft instruments were calibrated for instrument error. The pressure instruments were calibrated with mercury and water manometers of laboratory quality. The temperature gages were calibrated against liquid-filled thermometers with calibrations traceable to the National Bureau of Standards. The aircraft static-pressure system was calibrated for position error using a trailing-cone static-pressure source. No calibration of the total-pressure system was performed since the use of a Kiel-tube probe made such a calibration unnecessary. The aircraft pressure systems were balanced and leak checked periodically during the program.

The pressure transducer was calibrated against a Betz manometer. All pressure connections were checked for leakage following each change in test-probe configuration. Although a ground check on the balance of the pressure transducer system was not performed, an in-flight check of system balance was provided by connecting a Kiel tube to the test-pressure side of the Scanivalve. The connecting tubing was of the same diameter and length as used with the other test pressure source connections, and an in-flight pressure reading, on this data channel, other than zero would be an indication of a lack of balance in the pressure measurement system. The in-flight null readings were in agreement with the corresponding ground readings. These

in-flight null readings were also used in data reduction to compensate for the apparent drift of the pressure transducer output.

The hot-film probe was calibrated in a commercially available free-jet calibration chamber. The chamber differential pressure was measured with a Betz water manometer. Ambient pressure was obtained from the aircraft altimeter. The calibration temperature was obtained from the mercury thermometer supplied with the calibration chamber. The anemometer and related instrumentation, used for the calibrations, were the same as used during the test flights. Additional aircraft equipment normally used during the test flights were in operation during the hot-film calibration to prevent possible electrical interference effects. Aircraft battery power was used during these calibrations. Since the DC-powered anemometer did not have a probe cold-resistance measuring capability, the cold resistance was obtained with an AC-powered system before and after the probe calibrations. All cold-resistance measurements were made with the flight-test probe leads and included the lead resistance of .31 ohm. Two flight calibrations were also conducted. For these calibrations the probe was mounted, inverted, on the internal, traversing probe holder with the holder in the extended position. The static pressures were used to compute the local velocity for each calibration point.

The operation of the calibration chamber was dependent on a well regulated air supply to provide the desired plenum pressure. The normal shop or flight-test-hanger air supply was used in conjunction with a pressure regulator. This was not a completely satisfactory arrangement because of uncontrolled variations in the supply line pressure and the relatively slow response of the Betz manometer. Control was more of a problem at the lower calibration velocities where the low flow rate adversely affected the performance of the pressure regulator. Alternate calibration chambers are available which may represent a more suitable piece of equipment for operations outside the laboratory.

Probe cold-resistance measurements were also made in an environmental chamber to provide a measurement of the probe temperature coefficient of resistivity. Ambient temperatures from $-74^{\circ}C$ to $+110^{\circ}C$ were tested on some of the probes used during the test program. A small calibration tunnel was also made to allow hot-film probe calibrations to be performed in the environmental chamber, but because the cooling phase of the chamber was accomplished by means of expanding liquid CO_2 through an orifice into the chamber, the data obtained in an atmosphere of unknown CO_2 concentration were questionable. Additional comments pertaining to the calibration data are found in the appendix.

The determination of the height above the glove surface for the total-pressure tubes on the boundary-layer rakes was made by photographing the rake with two 0.01-inch steel scales held in place on each side of the rake and in the plane of the leading edges of the tubes. The very small depth of field available, with the lens and setting used for these photographs, prevented any significant discrepancy between the plane of the scales and the plane of the leading edges of the tubes. Enlarged prints provided true scale resolution of the order of ± 0.0015 inch.

For the traversing, total-pressure and hot-film probes, the probe height was evaluated using feeler gages and gage blocks. The feeler gage gave the

distance to the lower surface of the probe, and the distance to the center of the opening (total-pressure probe) or one-half of the rod diameter (hot-film probe) was added to the feeler gage dimension. Calibration curves in terms of the ratio of output to excitation voltage, for the linear potentiometer, or counts versus probe height were used. The dimensions of the wake rake and the position of the self-aligning, traversing, wake probe were determined with 0.01-inch steel scales. The self-aligning probe was replaced with a fixed pointer for the position measurements.

An evaluation of the accuracy of the total- and static-pressure measurements obtained with the self-aligning, traversing, wake probe in a uniform flow field was obtained by means of an in-flight calibration of the probe. The probe was mounted on a nose boom attached to the TG-3 glider. The probe position was about 6.0-feet forward of the nose and pressures were measured using sensitive airspeed indicators. The data indicated that the pressure errors, in a uniform flow field, were within the accuracy of the pressure measuring system used for the wake measurements.

ACCURACY

The adjustment of aircraft ballast during the test program maintained the aircraft gross weight within $\pm$10.0 pounds and the center of gravity within $\pm$0.1 inch of the nominal values of 1580.0 pounds and 18.0 inches, respectively.

In spite of the efforts to control the environment of the pressure transducer, zero-shift problems were experienced with the pressure measuring system. Although the zero shifts measured during the test program were significant, the shifts found on any given flight were usually on the order of $\pm$0.01 volts. In-flight pressure null readings were obtained on all flights, usually during each data run, and these values were always consistent with ground null readings taken before and after each flight. On a few of the flights the zero shift, over the duration of the flight, was larger than $\pm$0.01, but in-flight null data were available and the measured shift on a given run was still within the $\pm$0.01-volt band. No significant change in the transducer sensitivity was associated with the zero shifts. Data reduction was accomplished using the best estimate of the zero-pressure voltage for each data run. Compilation of all of the pressure transducer calibrations, reducing the voltmeter output by the zero-pressure voltage, demonstrated a static error band of $\pm$0.4 pounds per square foot. This error band included all of the calibration data points. This demonstrated accuracy represents the complete pressure measurement system as used in this test program. The digital readout and the use of a digital computer for data reduction minimized the probability that additional errors were generated in processing the pressure data.

Although extreme care had to be exercised when calibrating the hot-film probe position, the use of feeler gages seemed to provide the most accurate means of calibration. With this method the calibration height is considered to be accurate within $\pm$0.001 inch near the surface. Accuracy was less at distances away from the surface because of the need for using gage blocks

as well as the feeler gages. Manipulating these items on the slightly curved wing surface increased the difficulty of the calibration, and it is estimated that the errors are as much as ± 0.003 inch. Fortunately, dimensional accuracy near the outer edge of the boundary layer is not as important as it is near the surface because of the shape of the velocity profile. Considering the position accuracy of the calibration data and the least significant value obtained from the digital volt-meter, the maximum estimated test-data position error for the internal, traversing probe holder is ± 0.003 inch near the surface and ± 0.008 inch at the outer limits of the holder travel. For the counter system, the occurrence of an occasional extra count resulted in a progressive shift in the probe position calibration. The cause of this problem was never fully identified although it was known that following an improper, position-motor-control sequence would produce extra counts. Compensation for this shift was obtained through repeat calibrations, but there was always some degree of uncertainty associated with when the extra counts were introduced. The final test-position accuracy for the external, traversing probe holder is estimated to be ± 0.003 inch near the surface and ± 0.005 inch near the maximum outward travel of the holder. The positions of the boundary-layer rake total-pressure tubes are considered to be accurate within ± 0.002 inch. This accuracy includes the scale resolution on the enlarged photographs and possible misalignment in positioning the scales for the photographs. The relative positions of the wake probe measurements are considered to be accurate within ± 0.01 inch. It should be noted that the angular deflection of the self-aligning-wake-probe head was not measured during this program. Assuming a nominal deflection of 10.0°, a change in downwash angle of 2.0° would represent a change in the vertical position of the tip of the probe (i.e. the total-pressure tap) of 0.08 inch.

A statistically significant amount of data were obtained on the local velocities measured at the test position during the test program. These measurements included the ability of the pilot to hold the desired equivalent airspeed, the accuracy of the sensed pressures, and the accuracy of the measuring and recording system. Based on 64 static-pressure measurements, the mean, equivalent velocity at the test position was 160.0 feet per second. The standard deviation was 1.35 feet per second. Interpreted in terms of flight velocity, this indicates a standard deviation of 0.7 miles per hour about the desired equivalent flight velocity of 91.4 miles per hour.

The measurement of the ambient temperature with the standard outside-air-temperature gages was not as successful as was anticipated due to problems with instrument lag, hysteresis and reading error. The final values used in the data reduction calculations are estimated to be within $\pm 2^{\circ}C$ of the true ambient temperatures.

Discussions pertaining to the accuracy of the hot-film and wake measurements are found in the Results and Discussions section.

DATA REDUCTION

Instrument error and position error corrections were applied to all of the test data where applicable.

The data reduction applied to the pressure transducer data utilized the best estimate of the zero-pressure output voltage for each data run. This value was based on the ground measurements made before and after each flight and the in-flight measurements discussed in the Calibration section. No direct correction was made for the small, observed shift in the digital voltmeter calibration, but such a shift was also present in the zero-pressure voltage and was, therefore, taken into account.

The data reduction for the probe position data was based on a curve fit to the calibration data. A straight line was used with the internal, traversing probe holder and the self-aligning, traversing, wake probe; a trigonometric curve fit was used with the external, traversing probe holder. The trigonometric curve fit utilized the known distance from the probe holder pivot to the probe.

The fluid properties used in reducing the hot-film data were based on the measured local conditions. The thermal conductivity was computed with the equation

$$\kappa = 0.0141 \left(\frac{T_g}{273}\right)^{0.87}, \quad \frac{\text{BTU}}{\text{hr-ft-}^{\circ}\text{F}} \tag{1}$$

and the dynamic viscosity was computed using

$$\mu = 0.3592 \times 10^{-6} \left(\frac{T_g}{273}\right)^{0.75}, \quad \frac{\text{slug}}{\text{ft-sec}} \tag{2}$$

where T_g is in $^{\circ}$K. Both of these equations give values that agree within 4 percent of the tabulated data found in references 6 and 7. The specific heats for air were obtained from reference 8. The molecular mean free path for air was computed using

$$\lambda = \nu \left(\frac{\pi}{2RT}\right)^{0.5}, \quad \text{ft}$$

which is based on the equation used in appendix E of reference 9. The gas or film density was computed with

$$\rho = \frac{0.022873p}{T}, \quad \frac{\text{slugs}}{\text{ft}^3}$$

where p is in inches of mercury.

The hot-film probe data reduction used the calibration equation which

is an extension of King's Law (Method 2 in appendix)

$$\frac{W}{T_W-T_g} = 0.003351\ (\rho_f u_t)^{0.4593}$$

and was obtained from the calibration data given in the appendix. The sensor power was computed with

$$\frac{W}{T_W-T_g} = \frac{3.4937(E_b^2-E_{bo}^2)\ (R_o-0.31)}{(40+R_o)^2(T_W-T_g)}$$

where

$$E_{bo}^2 \sim T_f^{0.41}(T_W-T_g)^{1.1}$$

was used to correct the value of zero-velocity bridge voltage, obtained on the ground, to flight conditions. The sensor operating temperature (T_W) was determined from the measured probe cold resistance (R_1) and the selected probe operating resistance (R_o) with

$$R_o = R_1(1 + 0.001767\ (T_W-25))$$

The drag coefficient calculations used Jones' method where

$$C_d = \frac{2}{c}\int_{-\infty}^{\infty}\left(\frac{(p_t'-p)-(p_t'-p_t)}{(p_t'-p')}\right)^{0.5}\left(1-\left(1-\frac{(p_t'-p_t)}{(p_t'-p')}\right)^{0.5}\right)dy$$

In terms of the pressure coefficients, this equation becomes

$$C_d = \frac{2}{c}\int_{-\infty}^{\infty}(C_{p_t}-C_p)^{0.5}(1-(C_{p_t})^{0.5})\ \ dy \qquad (3)$$

The free-stream dynamic pressure ($p_t'-p'$) value was 21.36 pounds per square foot and the reference chord was 60 inches.

RESULTS AND DISCUSSION

The test results obtained during this program are presented and discussed on the following pages. For the boundary-layer measurements the results are presented in terms of equivalent velocity versus distance above the glove surface and compared to a reference velocity profile. Velocity, rather than velocity ratio, is used because it is felt that the significance of the differences between probes is made more apparent with this form of presentation. The use of velocity ratio, particularly when the local reference

velocity is determined in the presence of the probe, often completely masks the interference effects of the probe and can provide erroneous confidence in the test results. The equivalent velocity is used since the continously changing test altitude, associated with the glider test program, required that the test flight conditions be defined in terms of a constant, equivalent, flight velocity. The use of a constant, equivalent, flight velocity also reduced the variation in test Reynolds number with altitude as compared to the use of a constant, true, flight velocity. For the duration of this test program the test Reynolds number per foot, based on the free-stream velocity, was between 0.7 and 0.9 million. The reference profile, discussed in the next subsection, is used to prevent excessive clutter on the figures and to eliminate confusion resulting from the random scatter present in any one experimental profile that might be used as a reference. Probe interference is evaluated in terms of the spanwise variation in local velocity across the glove at the test position.

The glove flow field is assumed to be two-dimensional, and the test data supporting this assumption are presented in figures 15 and 16. Figure 15 shows the chordwise pressure distribution in terms of the pressure coefficient versus the surface distance forward of the glove trailing edge. Figure 16 gives the corresponding velocity distribution. Data for the two static-pressure taps, located 1.0 inch to each side of the test position, are also shown in these figures. These data represent the glove with no probes, other than the single, permanent, total-pressure probe, mounted on the surface.

Reference Boundary-Layer Profile

The evaluation of the performance of various boundary-layer probes requires that the resulting test data be compared to some standard or reference measurements. Hopefully, the reference measurements will represent the correct velocity profile with there being no question as to possible errors due to wall-probe interference or turbulent velocity fluctuation effects. Unfortunately, all presently used probes are subject to some form of criticism when used to measure turbulent-boundary-layer velocity profiles. With a flight-test program there is the added complication of possible erroneous velocity profiles, even from an ideal probe, due to small changes in the flight conditions. For these reasons it is considered desirable to use a reference profile that is related to the data obtained from the "best" probe tested and is also based on the current state of the art in turbulent-boundary-layer prediction methods. The existence of a large number of static-pressure measurements, taken at the test position, allows the identification of the most-probable local velocity outside of the boundary layer at the test position (local outer velocity). The reference profile should also include this local outer velocity as an outer boundary condition.

Of the probes tested, the internal, traversing, total-pressure probe is considered to be the device with the least chance of causing interference errors. Having selected this probe as the reference ("best") probe, the next step in providing the reference profile is to match the turbulent-boundary-layer prediction method equations to the reference-probe test data and the most-probable local outer velocity. A preliminary, hand-faired profile was first constructed through four sets of reference-probe data and the

local outer velocity of 160.0 feet per second. Values of boundary-layer thickness (δ = 0.555 inch at 99 percent of the local outer velocity), displacement thickness (δ_1 = 0.1095 inch), and momentum thickness (δ_2 = 0.0744 inch) were obtained from this preliminary profile. A mean pressure altitude of 5,000 feet and an ambient temperature of 17°C were used to relate the equivalent velocities to the required true velocities. The boundary-layer shape parameter (H_{12} = 1.472) and Reynolds number ($N_{Re(\delta_2)}$ = 5861) were used with the equation of Felsch, Geropp and Walz (reference 10) to determine a preliminary estimate of the skin friction coefficient (C_f = 0.002425). The following equation was used

$$C_f = 0.058\ (0.93-1.95\ \log_{10}H_{12})^{1.705}/(N_{Re(\delta_2)})^{0.268}$$

The resulting preliminary value of the friction velocity (u_τ) was 6.1319.

The turbulent-boundary-layer prediction method used is due to Coles (reference 11) and assumes a two-parameter family of mean velocity profiles given by the equation

$$u/u_\tau = f(yu_\tau/\nu) + \Pi w(y/\delta)/K$$

where

$$f(yu_\tau/\nu) = (\ln\ (yu_\tau/\nu))/K + C \qquad \text{(law of the wall)}$$

$$w(y/\delta) = 2\ \sin^2\ (\pi y/2\delta) \qquad \text{(law of the wake)}$$

$$K = 0.41,\ C = 5.0$$

The friction velocity was reduced to a value of 5.994 for the final profile to give a slightly better fit to the test data near the wall. The final reference velocity profile, in terms of equivalent velocity, is then given by the equation

$$u = 13.2832\ \ln y + 130.7949 + 35.4262\ \sin^2(2.8303y)$$

where y is in inches. According to reference 11, this equation is not considered to be valid for values of y/δ greater than 0.9 or values of yu_τ/ν less than 50. These limits correspond to approximate values of y of 0.5 and 0.02 inch, respectively.

Although probe test data that agrees with this reference profile do not ensure a perfect probe, agreement does imply that the probe gives what it considered to be the best estimate of the correct profile for the glove test position.

Pneumatic, Boundary-Layer Probes

Internal, traversing, total-pressure probe. - Although the configuration of the internal, traversing, total-pressure probe did not represent the minimum-size probe that could be used, it was small and was not expected to produce any measurable interference with the flow field over the glove section. Figure 17 presents a comparison of the spanwise, velocity distribution, with and without the probe, in terms of the mean, local outer velocities. The presented velocities with the probe in place are the means of six sets of data. The average standard deviation for the four span locations was 1.32 feet per second. The probe was in the extended position, 0.90 inch away from the glove surface, for these measurements. The data representing no probe mounted at the glove test position are the means of ten sets of data. The corresponding test data gave an average standard deviation of 1.29 feet per second. No probe interference for the tested configuration is indicated by the data in figure 17.

The boundary-layer velocity profile data obtained with the internal, traversing probe from five separate flights are shown in figure 18. The reference profile is also shown in this figure. Although the test procedure was intended to minimize bias in the data, the local outer velocity tended to be below the mean velocity obtained from the static-pressure-distribution-flight data. These lower velocities were due to the higher static pressures measured on the test flights and must be attributed to the flight velocity being lower than intended. The pilot did note that the average speed was possibly low by 0.4 miles per hour on Flight 61, but a consistently low flight velocity was not noted on the other test flights of this probe. The total pressure measured outside of the boundary layer with the test probe was equal to the free-stream total pressure. While the reference profile was based, in part, on these test data, the good correlation between the test data and Coles' velocity distribution equation is still considered to be significant.

Straight, boundary-layer rake. - The spanwise, mean-local-outer-velocity distribution presented in figure 19 shows that there is some interference due to the presence of the straight rake. These data represent the mean values obtained from eight sets of measurements. These measurements displayed an average standard deviation of 1.25 feet per second. The local velocity indicated by the rake static-pressure tube is also shown in this figure. The interference is indicated by the difference of 3 feet per second in the local velocity shown by the outer (11.25 inches to each side of the test position) pressure taps as compared to the pressure taps near the test position. It would appear to be fortuitous that the pressure taps near the rake gave local velocities within 1 foot per second of the mean value of 160 feet per second obtained in the absence of any probes on the glove section. The lower velocity given by the rake static-pressure tube is attributed to tube misalignment. Test data showing the sensitivity of the static-pressure tube to tube misalignment are not available for this probe, but the proper alignment of the static-pressure tube is considered to be one of the significant disadvantages of the device. The static-pressure tube is for installations that do not allow the installation of local, flush, static-pressure taps.

Boundary-layer velocity profiles, obtained with the straight rake, are

compared to the reference profile in figure 20. The mean static pressure, obtained from the two static-pressure taps located 1.0 inch on each side of the rake center line during the actual profile-measurement test runs, was used for these velocity calculations. Free-stream total pressure was obtained by the outer total-pressure tubes. As mentioned in the preceding paragraph, the small error in the measured static pressure is somewhat misleading in terms of probe interference, but the results were consistent for these tests. Different static-pressure-tap locations could give less favorable results. The correlation with the reference profile is comparable to that obtained with the internal, traversing, total-pressure probe.

Curved, boundary-layer rake. - The curved, boundary-layer rake was intended to position a relatively large number of total-pressure tubes near the surface while allowing the use of tubing with an adequate internal diameter. The tested configuration could benefit from efforts to reduce the obstruction presented to the flow, but it was considered to be representative of boundary-layer rakes that are often used. Also, this rake was available for use in this test program. The flow interference introduced by the curved, boundary-layer rake is shown in figure 21. The presence of the curved rake resulted in a spanwise difference in the mean, local, outer velocities of approximately 6 feet per second. The rake static-pressure tube gave the same value of local velocity as the two flush static-pressure taps located near the rake. These data are the means of six sets of measurements which gave an average standard deviation of 1.43 feet per second.

The boundary-layer velocity distributions obtained with the curved rake are shown in figure 22. As with the straight rake, the velocities were calculated using the mean static pressure obtained from the pressure taps located 1.0 inch to each side of the test position. The lower, local, outer velocity, associated with the static-pressure measurements, is illustrated by the comparison with the reference profile. The free-stream total pressure was measured by the rake outer total-pressure tubes. The use of the static pressures measured at the outer (11.25 inches to each side of the test position) flush taps would provide satisfactory correlation with the reference profile.

Hot-Film Anemometer

General comments. - The test program objectives, as defined in the Introduction section, were expanded somewhat in the case of the hot-film probe because of past problems with efforts to use hot-wire equipment on flight-test vehicles at Mississippi State University. These earlier efforts involved the measurements of the mean velocity profile of the turbulent boundary layer on the wing of a high-lift L-19 aircraft. The resulting test data gave very poor agreement between the local outer velocity measured with the hot-wire probe and the velocity indicated by static-pressure measurements. These data suggested that the functional representation of the calibration data did not adequately describe the heat-transfer characteristics of the wire. The present program, therefore, was arranged to investigate different functional representations of the calibration data in an effort to see if more consistent test results could be obtained. The scope of this test program did not allow any significant side studies into the characteristics of the hot-film probe, and the tests and

subsequent analysis were essentially restricted to trying to identify the appropriate constants for the probe and comparing the effectiveness of the different expressions used by other investigators to present calibration data.

It is realized that the measurement of mean velocities with a hot-film probe does not represent an efficient, or even desirable, utilization of this equipment. Other than for situations in which the extremely small hot-wire probes allow interference free measurements near a surface, it is the high frequency response of the hot-film or hot-wire probes that makes them unequaled for boundary-layer work. The emphasis given to the mean velocity measurements in the present program is predicated on the demonstrated accuracy in the mean measurements, where data can be checked against other probe results, being a prerequisite to having confidence in the non-steady measurements.

In the interest of consistency and to spare the general reader the task of reading through more detail then he may wish, the discussion of the hot-film probe measurements has been restricted to the consideration of probe interference and the agreement with the reference profile. A more detailed evaluation of the relative merits of the various methods of presenting the calibration data, consideration of changes in probe resistance, and other efforts to improve the accuracy of the hot-film measurements are found in the appendix to this report.

Internal, traversing, hot-film probe. - The evaluation of the probe interference, in terms of the spanwise variation in mean, local outer velocity, for the internal, traversing, hot-film probe is shown in figure 23. The data are for the probe in the extended position and represent the means of five sets of data that gave an average standard deviation of 1.70 feet per second. Since this probe configuration differed from the corresponding total-pressure probe only by the addition of the hot-film probe, no significant interference was anticipated. No probe interference is indicated by the data in figure 23.

The boundary-layer velocity profile data obtained with this probe are presented in figure 24. The data scatter is of the order of ± 9 percent and gives a mean, local outer velocity of 158.8 feet per second. Based on the rate of change of u_e with respect to the sensor cold resistance used in data reduction, a significant portion of the scatter shown in these data could be attributed to the value of cold resistance used, see the appendix. The test-data profile shape appears to be in agreement with the reference profile.

External, traversing, hot-film probe. - The spanwise variation in mean, local outer velocity obtained with the external, traversing, hot-film probe is shown in figure 25. These data are the mean values obtained from nine sets of data accumulated over six test flights. The average standard deviation for the four spanwise locations was 1.09 feet per second. These measurements were made both with the probe in the extended position and near the surface with no differences in the data noted. There appears to be little interference produced by the presence of the probe.

Figure 26 shows the comparison between the velocity profile data obtained with the external, traversing, hot-film probe and the reference profile. The

local-outer-velocity scatter is ±6 percent and can again be partially attributed to the measurement of the sensor cold resistance. In general, the profile shapes are consistent with the reference profile.

Wake Probes

The values of the total drag coefficient obtained with the three wake probes tested in this program are all within the range of drag coefficient estimated from the data given in reference 12 for smooth and rough airfoils. Each of these devices exhibited either deficiencies that introduced errors into the resulting values of drag coefficient or demanded accuracies from the pressure measuring system in excess of the demonstrated capabilities of the equipment. The best estimate of the correct drag coefficient would seem to be the value given by the wake rake and corrected for apparent static-pressure measurement errors (C_d = 0.0103). The integrating wake rake gave a value of 0.0102. The self-aligning wake probe gave a drag coefficient of 0.0086. The wake rake and integrating wake rake were tested at four angles (the forward end of the rake inclined upwards 0, 5, 10 and 15 degrees) of inclination with respect to the fuselage reference line. No consistent changes were noted in the drag coefficients determined at these various angles.

Self-aligning, traversing, wake probe. - The configuration of the self-aligning, wake probe was intended to provide a probe which would give more accurate static-pressure measurements than were realized from previous tests of other traversing wake probes. The probe head size was larger than was desirable but was determined by the need to bring the pressure line through the probe pivot bearing while maintaining free movement of the probe head. Free-stream calibrations made on this probe gave pressure position errors within the accuracy of the present pressure measuring system.

A typical set of static-pressure measurements made in the wing wake with the self-aligning, wake probe is shown in figure 27. Other pressure data to be discussed in the following paragraphs are also presented in this figure. The data are presented in terms of the pressure coefficient as a function of vertical position. The probe height values have been adjusted to put the center of the wake at 2.0 inches. The solid line, shown in figure 27, represents the value of static pressure obtained from the figures in reference 13. The approximate agreement with the values given by reference 13 would seem to indicate that the static-pressure measurements from the self-aligning probe are reasonable. No better reference static pressure is available at this time.

A typical set of total-pressure measurements made with the self-aligning, wake probe is presented in figure 28. A typical set of wake-rake total-pressure measurements is also shown in this figure for comparison. The wake-rake values are considered to be the most reliable values available. Three areas of disagreement between the two sets of test data are shown: (1) The free-stream total pressure was not measured by the self-aligning probe outside of the wake, (2) the nominal width of the total-pressure profile given by the self-aligning probe was somewhat narrower than the width given by the wake rake, and (3) the total-pressure loss at the center of the wake was greater with the self-aligning

probe than with the wake rake. Test data extending farther into the free-stream were obtained, but these data are not shown in order that a reasonable scale can be maintained in the figures. These omitted data were in agreement with the outer values shown in this figure. In light of the lack of total-pressure error found in the free-stream probe calibration, the apparent errors in the total pressure measured by the self-aligning probe are thought to be due to the probe head size and the flow curvature present in the wing wake. The estimated distance between the aerodynamic center of the stabilizing fins on the self-aligning probe and the total-pressure tap was 3.5 inches, and the total-pressure tap diameter was 0.032 inch. Flow curvature would result in some shift in the location of the stagnation point on the probe and could produce the reduction in total pressure noted in figure 28. It is not obvious that this effect would explain the apparent narrowing of the indicated wake width shown, but no other explanation for this phenomenon can be offered. Modification of the total-pressure tap opening could possibly eliminate the errors in the measured total pressure.

A plot of the variation of the drag-coefficient momentum function (see integrand of equation (3)) as a function of the vertical distance through the wake is shown in figure 29 for a typical set of measurements with the self-aligning probe. The corresponding values obtained with the wake rake are also shown in this figure. The differences between the two sets of data are consistent with the corresponding differences shown in figures 27 and 28.

Wake rake. - The wake rake was equipped with three static-pressure tubes. Two of the static-pressure tubes were located near the center of the rake and one was mounted at the top of the rake. Data obtained from the top static-pressure tube were not usable due to some unknown failure in the pressure connections. A typical set of static-pressure data obtained from the two remaining static-pressure tubes is shown in figure 27. The dash line in figure 27 is the assumed value of static pressure used in reducing the wake-rake data. With only the self-aligning probe static pressures and the static pressure obtained from reference 13 as a basis for comparison, the static pressure obtained from the wake rake is considered to be in error. No consistent trend in the variation of measured static pressure with rake inclination angle was noted. Total-pressure measurements from the wake rake are assumed to be correct and are shown in figure 28.

The drag coefficient obtained using the measured wake-rake static pressure was 0.00906 for Flight 63. The data shown in figure 29 were integrated to get this value. If a static-pressure coefficient of 0.1 is used, rather than the assumed value of 0.207, a drag coefficient of 0.0103 is obtained. This is considered to be the more realistic value.

Some difficulty was experienced in achieving the proper vertical location of the probe with respect to the airfoil wake. The wake-rake configuration was intended to provide an adequate concentration of total-pressure tubes in the region of the wake while covering a sufficient region outside the wake to ensure that free-stream conditions were being reached. As can be seen in figure 29, misplacement of the rake can result in marginal definition of the wake region if the rake is intercepted by the wake where the larger, total-pressure-tube

spacing exists. With the major part of the momentum defect occurring over a distance of about 2 inches, it is likely that at least one trial data run would normally be required before the proper centering of the wake rake could be obtained. Only one run was made at each rake inclination angle for this test program. Additional runs would have been desirable to obtain better rake position.

Integrating, wake rake. - Although the value of the drag coefficient obtained from the integrating wake rake is in good agreement with the corrected value obtained with the wake rake, this correlation is fortuitous due to the basic accuracy of the pressure measuring system. A 0.01 volt change in the output of the digital voltmeter results in a 10 percent change in the computed drag coefficient. This small change in voltage represents a 0.118 pounds per square foot change in reservoir pressure. This is a consequence of the rather large rake length campared to the wake width. Again, the ability to locate the rake in the wake dictates the size of the rake. If a smaller rake were used, runs at different rake locations would be required to insure that the full wake width was being measured. There is also a significant possibility for error in determining the various correction factors, given in reference 13, that must be used with this method for determining the drag coefficient. In computing the drag coefficient, the necessary correction factors were based on the static pressures measured with the self-aligning probe rather than the values of static pressure given in reference 13. A 3-percent increase in drag results from using the static-pressure values in reference 13. The compressibility correction of reference 13 was not used in the drag calculations. The entrance loss factor defined in reference 13 was not used because the resulting values did not appear reasonable.

CONCLUDING REMARKS

Reliable flight-test, boundary-layer-velocity measurements were obtained with the internal, traversing, total-pressure probe in conjunction with flush, static-pressure taps. The boundary-layer rakes appeared to give reasonable total-pressure measurements, but flow interference, due to the presence of the probe, made the determination of the correct local static pressure difficult. In addition to the problems with flow interference, the measurement of the static pressure with a static-pressure tube, rather than flush static-pressure taps, can introduce errors that are difficult to evaluate.

Based on the results of the present test program, the accuracy of the mean velocity data obtained with the hot-film anemometer equipment is less than the accuracy demonstrated by pneumatic probes and pressure transducers. Using equipment with the capability of measuring the probe cold resistance and probes with a reduced tendancy to change cold resistance with operating time, the accuracy of velocity measurements may be significantly improved.

The tested wake measurement devices exhibited various deficiencies that required judicious selection of the test data before reasonable values of drag

were obtained. The self-aligning, traversing wake probe demonstrated total-pressure measurement errors. Modification of the total-pressure tap may eliminate this problem. The wake-rake data indicate errors in the measurement of the static pressure. The integrating-wake-rake data gave a reasonable average value of drag, but the results were strongly influenced by the accuracy of the pressure measuring system. Changes in rake inclination angle of 15 degrees did not appear to affect the drag values obtained with the wake rake or the integrating, wake rake.

APPENDIX

EVALUATION OF A HOT-FILM PROBE AND RELATED EQUIPMENT

Probe Physical Characteristics

The 0.006-inch, hot-film sensors used in this program provided a relatively rugged probe as compared to the normally used hot-wire sensor. A total of seven sensors were used in this test program. Three of these sensors were destroyed through efforts to operate the sensor at the highest possible surface temperature. One sensor was broken when the probe was inadvertently driven into the glove surface, and two sensors were destroyed because of electrical grounding problems in the instrumentation system. The remaining sensor accumulated approximately 20 hours running time and was the sensor which provided most of the test data presented in this report. The sensors could be carefully touched with the feeler gage without breakage, and there was no significant accumulation of dirt or oxidation during the extended test operation. Although there was a significant change in cold resistance with operating time, the calibration data did not seem to indicate any consistent changes with operating time as long as the proper values of resistance were used in the appropriate power expression.

The mounting of the hot-film sensors to the sensor support arms required a significant amount of care, but no losses were experienced during the mounting operation. The sensors came in continuous lengths containing from 7 to 10 sensor elements, and the sensor elements had to be severed for use. The solder used to attach the sensors to the arms had a melting temperature slightly in excess of 205°C. At 205°C the solder was soft to the touch but not truly molten.

The advertised maximum operating temperature of these hot-film sensors is 500°C with a recommended operating temperature, in air, of 275°C. Since the higher operating temperatures reduce the effect of ambient temperature changes, both on the temperature loading term and on the computed fluid properties (if the so-called film temperature is used), the initial testing was conducted at an operating temperature of 400°C. The operating characteristics were quite erratic at this temperature with only one out of three sensors giving consistent results. One sensor was operated for a total of about 4 hours before the cold-resistance measurements became irregular and the sensor was discarded. The remainder of the tests were conducted using a nominal operating temperature of 300°C. The operating temperatures quoted in this report are based on the measured resistance change with temperature and represent a significant extrapolation of the test data. No estimate of the accuracy of these operating temperatures is offered.

The evaluation of the temperature coefficient of resistivity for the hot-film probe was accomplished in an environmental chamber. Ambient temperatures from -80°C to 150°C were obtained with some of the sensors tested. Problems with the electrical insulating material were experienced at the higher temperatures, and an upper limit of 80°C was used for the later test. The complete

probe as well as about 1.0 foot of the electrical leads were exposed to the chamber temperature. The laboratory anemometer, with integral cold-resistance measurement capabilities, was used for all of the cold-resistance measurements made during this test program. The resistance data obtained with the hot-film sensor are shown in figure 30 as a function of ambient temperature (for this test $T_o = T_w$). The lower set of data were taken when the sensor had accumulated about 2.5 hours of operation. The second set of data were obtained at the end of the test program after about 20.0 hours of operational usage. The straight lines passing through the two sets of data points are defined by the following equation.

$$R_o = R_1 (1 + 0.001767 (T_w - 25)) \tag{4}$$

R_1 is the cold resistance measured at an ambient temperature of 25°C and 0.001767 is the temperature coefficient of resistivity (α_{25}) for this particular sensor. A reference temperature of 25°C was used for convenience as this was the nominal ambient temperature found in the laboratory and in the flight-test hangar. It should be noted that the selected reference temperature does influence the resulting value of α. The relationship between the coefficient obtained at some other reference temperature and the value obtained at a reference temperature of 25°C, using the above functional relationship, is given by the following equation.

$$\alpha = \frac{\alpha_{25}}{1 + \alpha_{25}(T-25)}$$

Although the second set of data points shown in figure 30 is limited in number, they do imply that a constant value of α_{25} can be used for a given sensor as long as a current value of R_1 is available. The different levels of resistance for the two sets of data represent the increase in sensor resistance with operational usage. Values of α_{25} as high as 0.0022 were obtained for some of the sensors tested. The range of values for α_{25} obtained for individual sensors taken from a given length of sensor stock cannot be given because a record of the origin of each sensor was not maintained. The resistance values shown in figure 30 include the 0.31-ohm resistance of the 15-foot length of coaxial cable used to connect the probe to the anemometer unit. The scatter in the cold-resistance data shown is typical of the variations found throughout the test program. Some of this scatter can be attributed to small changes in the resistance of the cable connection each time a connection was changed, but cold-resistance variations were noted at times when no changes were made in the connections. The anemometer unit could resolve the cold resistance to within 0.01 ohms, but in a few instances resistance changes of as much as 0.1 ohms were recorded after a running time of 15 or 20 minutes.

The change in cold resistance for one hot-film sensor as a function of the approximate operating time is shown in figure 31. Where necessary, the values of cold resistance were corrected to an ambient temperature of 25°C. Time records were not kept on the operating time of the probe, and the values shown in this figure are based on an estimated running time required to do a calibration

or flight. The later data points were more accurately defined. The overall operating time could be in error by as much as 50 percent, but the data are shown to illustrate the well-defined increase in cold resistance with operating time. Using an operating resistance of 11.32 ohms, the change in cold resistance over the period of time the sensor was used represents a change in the computed sensor operating temperature from 318°C to 246°C. It should be noted that the manufacturer of these hot-film sensors ages the more complicated factory-mounted probes for as much as 45 hours to minimize changes in cold resistance. Such extended utilization of the test anemometer was considered to be questionable during this test, but future hot-film work would justify the construction of a simple bridge circuit to accomplish this aging operation.

Sensor Zero-Velocity Characteristics

The effects of free convection are normally neglected in hot-wire anemometer investigations. Justification for this omission is based on the product of the Grashof and Prandtl numbers being very small (i.e. $N_{Gr}N_{Pr}$ less than 10^{-4} according to reference 14). The low values of $N_{Gr}N_{Pr}$ correspond to very small wire diameters and, for a given temperature loading, represent low levels of heat dissipation. The wire diameter appears to the power of 3.0 in the numerator of $N_{Gr}N_{Pr}$ and the 0.006-inch diameter of the sensor used in this program represents an increase in this product by a factor of 28,100 over the often-used hot-wire diameter of 5 microns. At the nominal altitude and temperature of 5,000 feet and 17°C, the value of $N_{Gr}N_{Pr}$ is equal to 0.0752 for the 0.006-inch-diameter sensor. The level of power dissipation by free convection for this sensor size justified the consideration of free convection, or more correctly the change in free convection due to changes in ambient conditions, in the present program.

The approach taken was to base the power functions, used in presenting the calibration data, on the difference between the sensor power measured with a given flow velocity and the sensor power obtained with zero velocity rather than just use the sensor power measured at the given flow velocity. In this way the difference in the free-convection characteristics, due to changes in ambient conditions, were taken into account by direct measurement. This was straightforward for the ground calibration data, but the test probes did not provide the capability of shielding the sensor from the air flow in flight. For the flight test data it was necessary to measure the zero-velocity sensor power on the ground and then to correct these values to the flight-test conditions. The ground measurements were made before and after each flight with a box mounted over the probe to shield the sensor from the ground winds. In general the difference in the zero-velocity bridge voltage obtained before and after each flight was less than 0.04 volts (mostly associated with the cold-resistance change). The change in ambient ground conditions over the duration of the test flight was normally negligible.

The correction of the ground, zero-velocity power measurement to the flight conditions was made assuming that the power required to maintain the operating resistant of the hot-film sensor, with no flow, was defined by the free convection relations. According to data presented in reference 6, due to Nusselt and

W. J. King, the free convection characteristics of a horizontal cylinder are reasonably well represented by the Nusselt number being proportional to the product of the Grashof and Prandtl numbers to the 0.1 power (in the region of $N_{Gr}N_{Pr}$ between 10^{-4} and 1). With a constant set of anemometer conditions, the relationship between sensor power and the ambient air properties is given by the following expression.

$$\frac{E_{bo}^{2}}{\kappa(T_w-T_g)} \sim \frac{(T_w-T_g)\beta}{\nu_g^2}\ \frac{\nu_g \rho_g}{\kappa_g}^{0.1}$$

Using equations (1) and (2) and neglecting $(p_g)^{0.2}$, the zero-velocity bridge voltage is then given by the following relationship.

$$E_{b_o}^{2} \sim T_g^{0.41}\ (T_w-T_g)^{1.1}$$

The omission of this pressure term would not be justified if higher test altitudes were being considered. The apparent validity of this relationship for tests that do not involve a pressure change is illustrated in figure 32. These bridge-voltage values were obtained during the tests conducted to measure the sensor resistance change with temperature. The test results are for two different probes, and the solid curves represent the above relationship using a faired value of the test data at 25°C, for each set of data, as the starting point. As is indicated in the Calibration section, test data obtained at ambient temperatures below 0°C are subject to question because of the refrigeration system used in the temperature chamber.

The use of the zero-velocity bridge voltage in presenting the hot-film calibration data is discussed in the following paragraphs, but for the air velocities measured in this program, accounting for this quantity provides only small improvement in the calibration data. For lower velocity measurements or greater differences between calibration and test ambient conditions, the removal of the zero-velocity power may be a more worthwhile consideration.

Sensor Calibration

It is generally accepted that the heat transfer characteristics of the hot-film or hot-wire probe are defined in terms of relationships between Mach number, Knudsen number, Prandtl number, Nusselt number and Reynolds number. The Knudsen numbers experienced in this program were sufficiently small to allow the slip-flow considerations, related to the Knudsen number, to be neglected in the analysis of the hot-film test data. Appendix E of reference 9 uses the criteria

$$0 < \lambda/d < 0.01$$

for continuum flow. Considering a nominal pressure altitude and ambient temperature of 5,000 feet and 17°C, a value of 0.00051 is obtained for λ/d with the 0.006-inch-diameter sensor. For a constant equivalent velocity, the variation

of Mach number with altitude was less than 18 percent and the maximum Mach number was 0.169. This small level and variation in Mach number is considered to be negligible for the purposes of this program. With the Knudsen- and Mach-number effect neglected, the desired calibration presentation must now consider the three remaining parameters (N_{Pr}, N_{Nu} and N_{Re}).

The classic form of presentation for hot-wire calibration data is due to the work of L. D. King (reference 15). Based on potential flow theory, King described the heat transfer characteristics of a small heated cylinder with the equation

$$N_{Nu} = \frac{1}{\pi} + \frac{2}{\pi} (N_{Re})^{0.5} (N_{Pr})^{0.5}$$

where King's original nomenclature is replaced by the non-dimensional groups normally used in anemometer work. As King's equation is normally used for compressible flow (King's Law), where the theoretical constants are replaced by general constants and the variation in fluid properties other than density are neglected, the equation becomes

$$\frac{W}{T_w - T_g} = A + B (\rho_g u_t)^{0.5} \tag{5}$$

A more representative relationship, according to Hinze (reference 14), is due to Kramer and is given by the equation

$$N_{Nu} = 0.42(N_{Pr})^{0.2} + 0.57(N_{Pr})^{0.33}(N_{Re})^{0.5} \tag{6}$$

Although the work of Boltz (reference 9), did not extend to the values of Knudsen number found in the present program, his suggested equation, extrapolating to the lower values of Knudsen number, becomes

$$N_{Nu} = A + B(N_{Re})^{0.5} \tag{7}$$

For the range of Mach number and Knudsen number found in the present program, Laurence and Landes (reference 16) used the equation

$$\frac{N_{Nu}}{N_{Pr}^{0.3}} = A + B(N_{Re})^{0.5} \tag{8}$$

with the reservation that the temperature loading did change the value of B. Spangenberg (reference 17) also showed variations in the value of the slope of the calibration data due to temperature loading. His results would seem to be

of the form of Equation (6). The work of Collins and Williams (reference 18) used

$$N_{Nu}\left(\frac{T_f}{T_g}\right)^{-0.17} = A + B(N_{Re})^{0.45} \qquad (9)$$

where the effects of temperature loading were stated to be accounted for by the temperature ratio term.

The possible variations in the forms that can be used to present the calibration data are further complicated by the temperatures that the various authors used to evaluate the properties of the flowing air. Spangenberg and Boltz used the free-stream or stagnation temperature; Laurence and Landes, Collis and Williams and Hinze suggested the use of the film temperature which is the average of the free-stream and the hot-wire surface temperatures. Davies and Fisher, on the other hand, stated their justification (reference 19) for using the hot-wire surface temperature for computing the heat conductivity of the air while using the free-stream temperature for evaluating the other required air properties.

With these variations in calibration format as a background, the calibration data obtained in the present program were reduced and plotted in the following forms:

(Method 1) $$N_{Nu} = f\left((N_{Re})^{0.5}\right)$$

(Method 2) $$\frac{W}{(T_w - T_g)} = g\left((\rho_g u_t)^{0.5}\right)$$

(Method 3) $$\frac{CW}{T_g^{0.85}(T_w - T_g)} = h\left(\left(\frac{p_g u_t}{T_g^{1.78}}\right)^{0.5}\right)$$

Method 1 is consistent with equation (7). Method 2 represents King's Law (equation (5)), and Method 3 is based on equation (6) and is similar to equation (8). Method 3 is obtained from equation (6) by substituting for κ and μ, using equations (1) and (2) respectively, and neglecting the various constants of proportionality that evolve from the various terms and units in this equation.

The evaluation of the above expressions, in terms of the measured variables, was accomplished using the following equations

$$N_{Nu} = \frac{2.9535 \times 10^6 (E_b^2 - E_{bo}^2)\ (R_o - 0.31)}{(40 + R_o)^2\ (T_w - T_g)\ T_g^{0.87}}$$

$$N_{Re} = \frac{2138\ p_g u_t}{T_g^{1.75}}$$

$$\frac{W}{(T_w - T_g)} = \frac{3.4937\ (E_b^2 - E_{bo}^2)\ (R_o - 0.31)}{(40 + R_o)^2\ (T_w - T_g)}$$

except that the constant (3.4937) was not used with Method 3, and

$$\rho_g u_t = 0.022873\ \frac{p_g u_t}{T_g}$$

The voltage (E_b) is the recorded value with the voltage drop ratio (0.535) included in the constant terms. R_o is the operating resistance including the 0.31 ohm line resistance. The 40 ohms represents the resistance of the other leg of the active side of the anemometer bridge circuit. The temperatures are in ^oK and the pressure is in inches of mercury. For data reduction using film temperatures, rather than free-stream temperature, T_g was replaced by $(T_w + T_g)/2$. This substitution was not used in the temperature loading term $(T_w - T_g)$.

Only the calibration data based on film temperature and with the zero-velocity sensor power removed are shown in this report because they adequately represent the general character of the data obtained using the alternate forms of presentation. Data reduction using the alternate forms was accomplished and is discussed in the following paragraphs. Quantitative discussions of the scatter in the calibration data are based on the spread in the velocity-function data (i.e. $(N_{Re})^{0.5}$, $(\rho_g u_t)^{0.5}$ and $(p_g u_t / T_g^{1.78})^{0.5}$) evaluated at 90 percent of the maximum calibration data value for the power function (i.e. N_{Nu}, $W/(T_w - T_g)$ and $CW/(T_w - T_g)T_g^{0.84}$). The velocity-function data scatter is given as a percentage of the velocity-function value at the midpoint of the scatter band. This is an arbitrary criteria, but it does give a measure of the variation in velocity-function values that are possible with these calibration data for a value of the power function based on a given in-flight test measurement. It can be shown that the percent error evaluated in terms of $(N_{Re})^{0.5}$ is approximately equal to 0.5 of the percent error in terms of N_{Re} for the essentially linear calibration plots. For a given ambient condition, the percent error in N_{Re} is equivalent to the percent error in u_t and u_e.

Six sets of calibration data are presented in each of figures 33, 34, and 35. Two of these sets are calibration data obtained in flight and four are ground calibrations. Two of these ground calibrations were obtained immediately before or after the two in-flight calibrations. All data are for one hot-film sensor and were obtained using the same anemometer operating resistance. These calibrations represent a time span of slightly less than three months and an estimated sensor operating time of 17 hours. These sets of data represent the

largest variation between calibrations; all other calibration data, for this sensor, were within the spread of data shown. The pertinent values of resistance, temperature and density associated with these data are shown in the following table.

Calibration	R_1	R_o	T_o	T_w	T_f	T_w-T_o	ρ_o
	(ohm)	(ohm)	(^oK)	(^oK)	(^oK)	(^oK)	(slug/ft^3)
9/9/71	7.57	11.32	299.7	578.6	439.2	278.9	2.264×10^{-3}
11/3/71	7.92	11.32	292.7	541.2	417.0	248.5	2.330
11/11/71	8.08	11.32	293.4	525.6	409.5	232.2	2.331
11/11/71 (a) (FLT. 97)	8.08	11.32	282.3	525.6	404.0	243.3	2.084
11/22/71	8.14	11.32	286.0	519.3	402.7	233.3	2.387
11/22/71 (a) (FLT. 99)	8.14	11.32	274.0	519.3	396.7	245.3	2.095

(a) T_o and ρ_o are average values for the in-flight calibrations.

Calibration data presented in terms of Nusselt number as a function of the square root of Reynolds number (Method 1) are shown in figure 33. Although the pattern for the different sets of data is not without some contradiction, these data show a trend for the earlier calibrations to plot below the later calibrations. The previous table shows that the chronological order of the calibrations also represents data for increasing cold resistance, with the associated reduction in operating temperature, and a general reduction in ambient temperature. The in-flight calibration data for Flight 97 are noticeably displaced from the rest of the calibration data in this figure, as well as on figures 34, and 35. This may be the result of problems in measuring the sensor cold resistance. The spread in the calibration data is 12.9 percent. If the data for Flight 97 are neglected the spread is 8.7 percent.

If the ambient temperature is used in computing the fluid properties, rather than the film temperature, a slight reduction in the overall spread is achieved (12.2 percent). A slight reduction in data spread is also obtained if the zero-velocity sensor power is not removed from the calibration data (12.0 percent using the film temperature). Using the operating temperature, as suggested by Davies and Fisher (reference 19), results in a 16 percent spread of the calibration data. The method of Collis and Williams (equation 9) gives an overall spread in the calibration data of 13.5 percent.

Figure 34 gives the calibration data presented in accordance with King's Law (equation (5), Method 2). Except for the data from Flight 97, the sets of data are no longer spread out in a recognizable fashion. The overall spread is

7.7 percent with a value of 4 percent obtained if the results of Flight 97 are neglected. This form of presentation yields the minimum spread of calibration data and is the basis for the data reduction used in the text of this report. An overall spread of 9 percent is realized using ambient rather than film temperature. Not removing the zero-velocity sensor power gives an overall spread of 10 percent. The calculation of the heat conductivity of the fluid is not involved in King's Law, and the use of the operating temperature, as suggested by Davies and Fisher, is not applicable. Multiplying the power function by the term $(T_f/T_g)^{-0.17}$ gives an overall spread of 9.2 percent.

The use of Method 3 is demonstrated in figure 35. The spread in calibration data is very similar to that found with Method 1 and gives an overall spread of 12.3 percent with a spread of 6.6 percent obtained with the results of Flight 97 neglected. The variations on this method, involving the use of ambient temperature, the operating temperature, not removing the zero-velocity sensor power, and using the ratio $(T_f/T_g)^{-0.17}$, were not analyzed as the results would be similar to those found with Method 1.

The above calibration data results are summarized in the following table.

Variations	Method 1	Method 2	Method 3
T_f, $E_b^2-E_{b_o}^2$	12.9	7.7	12.3
T_f, E_b^2	12.0	10.0	----
T_g, E_b^2	12.2	9.0	----
T_w, T_f, E_b^2	16.0	----	----
T_f, $(T_f/T_g)^{-.17}$, E_b^2	13.5	9.2	----

The calibration curves obtained with any of these three methods deviate from a linear relationship and indicate that the power of u_t and N_{Re}, used in presenting the calibration data, should be somewhat less than 0.5. Using a least square fit to a power curve, the Method 2 results yield the equation

$$\frac{W}{T_w-T_g} = 0.003351\ (\rho_f u_t)^{0.4593} \tag{10}$$

The use of Method 2, with its total error band of 7.7 percent measured at a value of the power function $(W/(T_w - T_g))$ of 1.85×10^{-3}, results in potential errors in velocity of approximately ± 8 percent. This is excessive and indicates a need for improvements in test technique and in the understanding of the dependence of the sensor power on atmospheric conditions and anemometer settings. The significance of the correct measurement of the sensor cold resistance is

shown by considering the change in velocity, obtained at a given anemometer power, due to a change in sensor cold resistance. Using a calibration of the form

$$\frac{W}{T_w - T_g} = A\,(\rho_g u_t)^{B/2}$$

and equation (4), the derivative of the equivalent velocity with respect to the cold resistance is given by the following equation,

$$\left.\frac{\partial u_e}{\partial R_1}\right|_{E_{b_o}, E_b, R_o} = -1.2373 \times 10^4 \left(\frac{R_o}{R_1^2}\right)\left(\frac{1}{p_g}\right)\left(\frac{\rho_g}{\rho_{std}}\right)^{0.5}\left(\frac{1}{A}\frac{W}{(T_w - T_g)}\right)^{2/B}\left(1 - \frac{2}{B}\frac{(T_w + T_g)}{(T_w - T_g)}\right)$$

where the sensor power (W) and atmospheric conditions are constant. Using the constants (A and B) of equation (10), representative values of pressure, temperature, and resistance, and a value of 2×10^{-3} for the power function, a change in cold resistance of 0.01 ohm gives a change in equivalent velocity of 1.6 feet per second. In the present test program, where the cold resistance could only be measured before or after the flight and required changing connections from the airborne anemometer to the laboratory unit, changes in cold resistance of 0.1 ohm were measured over the duration of the flight. This uncertainty in cold resistance of ± 0.05 ohm corresponds to ± 8 feet per second potential error in equivalent velocity. With anemometer equipment incorporating a cold-resistance measuring capability, the cold resistance could be measured in flight and this problem would be significantly reduced. This is a probable cause for at least part of the differences shown between the two in-flight calibrations. Although the differences in cold resistance noted during the ground calibrations were generally much less than 0.1 ohm, the measurements made before and after the calibration of 11 November 1971 did give a change of 0.05 ohm.

REFERENCES

1. Keener, Earl R.: Accuracy of Pitot-Pressure Rakes for Turburlent Boundary-Layer Measurements in Supersonic Flow. NASA TN D-6229, 1971.

2. Saltzman, Edwin J.: In-Flight Use of Traversing Boundary-Layer Probes. NASA TN D-6428, 1971.

3. Burrows, F. M.: Equipment Used for Boundary Layer Measurements in Flight. COA Note No. 49, The College of Aeronautics, Cranfield, July 1956.

4. Roberts, Sean C.: A Flight Investigation of Profile Drag Measurements. Research Note No. 16, Aerophysics Department, Mississippi State University, December 1962.

5. Miley, Stan J.: A Catalog of Devices Applicable to the Measurement of Boundary Layers and Wakes on Flight Vehicles. Mississippi State University (NASA CR-116776), 1971.

6. Jakob, Max: Heat Transfer. John Wiley and Sons, Inc., 1949.

7. U. S. Committee on Extension to the Standard Atmosphere: U. S. Standard Atmosphere, 1962. U. S. Government Printing Office, 1962.

8. Keenan, Joseph H; and Kaye, Joseph: Gas Tables. John Wiley and Sons, Inc., 1948.

9. Boltz, Frederick W.: Hot-Wire Heat-Loss Characteristics and Anemometry in Subsonic Continuum and Slip Flow. NASA TN D-773, 1961.

10. Kline, S. J.; Morkovin, M. V.; Sovran, G.; and Cockrell, P. J.; eds: Proceedings, Computation of Turbulent Boundary Layers - 1968, AFOSR-IFP-Stanford Conference, Volume I, Methods, Predictions, Evaluation and Flow Structure. Thermosciences Division, Department of Mechanical Engineering, Stanford University, 1969.

11. Coles, D. E.; and Hirst, E. A.; eds: Proceedings, Computation of Turbulent Boundary Layers - 1968, AFOSR-IFP-Stanford Conference, Volume II, Compiled Data. Thermosciences Division, Department of Mechanical Engineering, Stanford University, 1969.

12. Abbott, Ira H.; von Doeroff, Albert E.; and Stivers, Louis S., Jr.: Summary of Airfoil Data. NACA TR 824, 1945.

13. Silverstein, A.; and Katzoff, S.: A Simple Method for Determining Wing Profile Drag in Flight. Journal of the Aeronautical Sciences, vol. 7, no. 7, 1940.

14. Hinze, J. O.: Turbulence. McGraw-Hill Book Co., Inc., 1959.

15. King, Louis Vessor: On the Convection of Heat from Small Cylinders in a Stream of Fluid. Phil. Trans. Roy. Soc. (London), Series A, vol. 214, no. 14, November 12, 1914.

16. Laurance, James C.; and Landes, L. Gene: Auxiliary Equipment and Techniques for Adapting the Constant-Temperature Hot-Wire Anemometer to Specific Problems in Air-Flow Measurements. NACA TN 2843, 1952.

17. Spangenberg, W. G.: Heat-Loss Characteristics of Hot-Wire Anemometer at Various Densities in Transonic and Supersonic Flow. NACA TN 3381, 1955.

18. Collis, D. C.; and Williams, M. J.: Two-Dimensional Convection from Heated Wires at Low Reynolds Numbers. Journal of Fluid Mechanics, vol. 6, 1959.

19. Davies, P. O. A. L.; and Fisher, M. J.: Heat Transfer from Electrically Heated Cylinders. Royal Society of London, Proceedings, Series A, vol. 280, 1964.

Figure 1. TG-3 research glider.

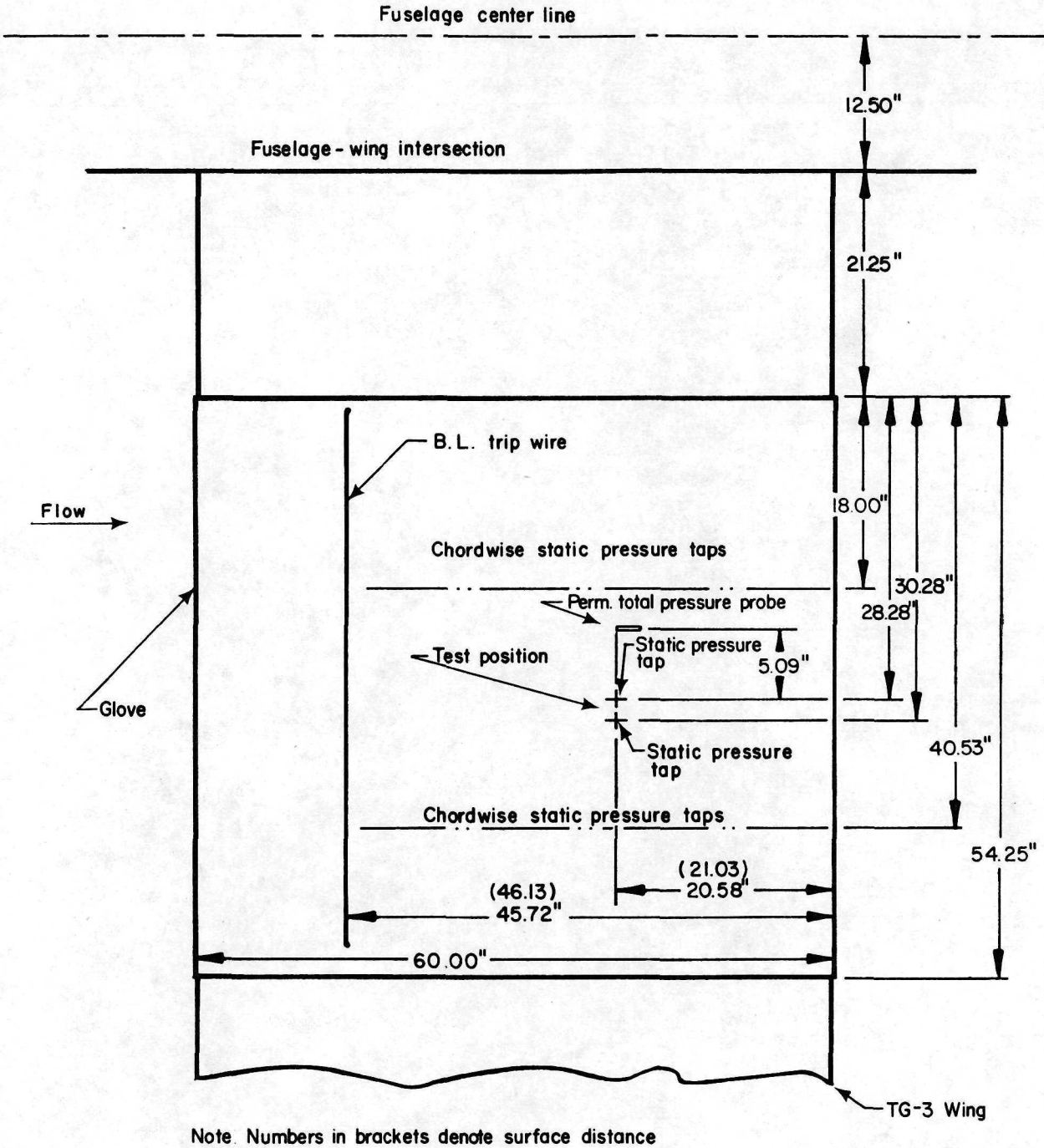

Figure 2. TG-3 glove test section.

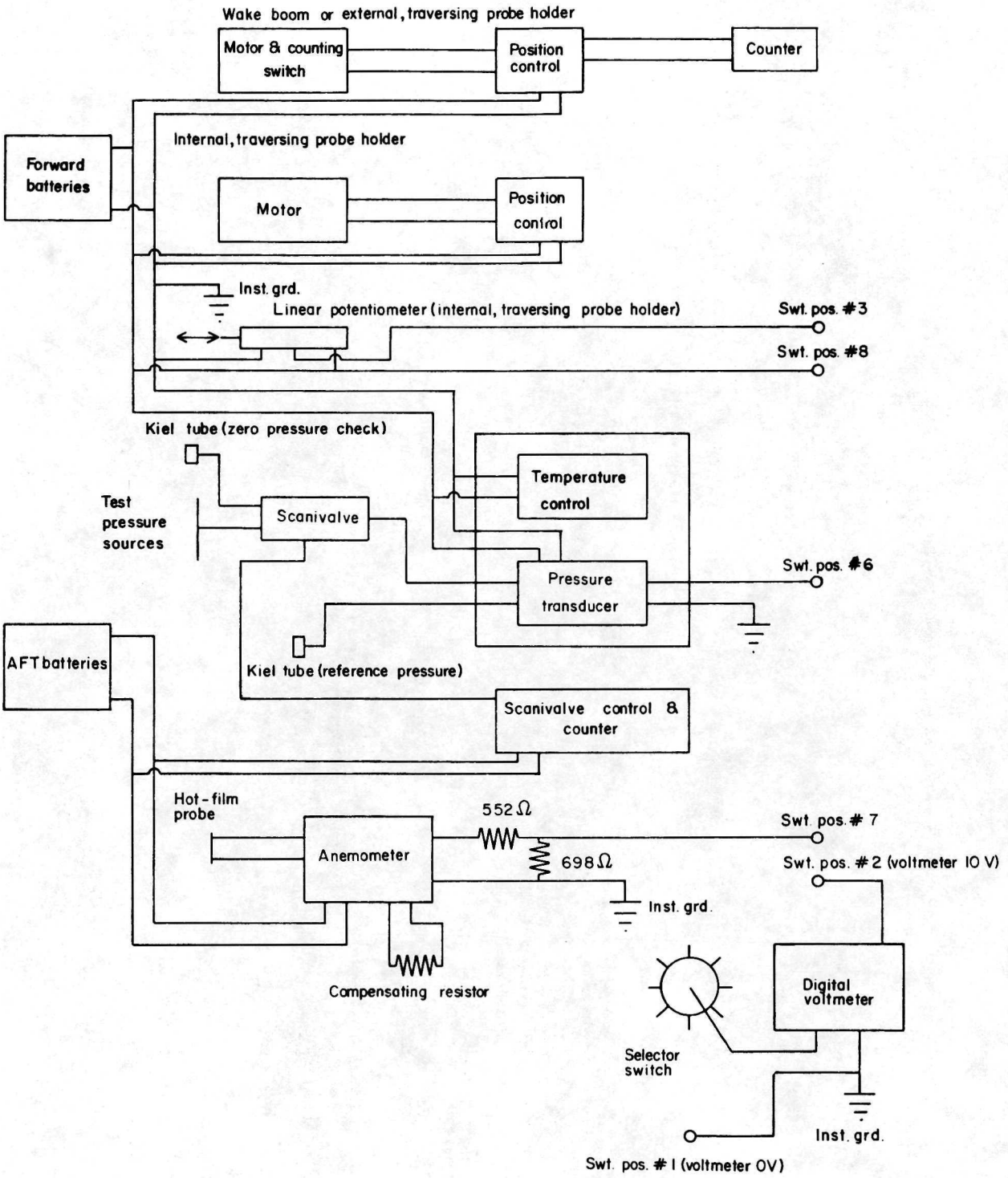

Figure 3. Instrumentation system schematic.

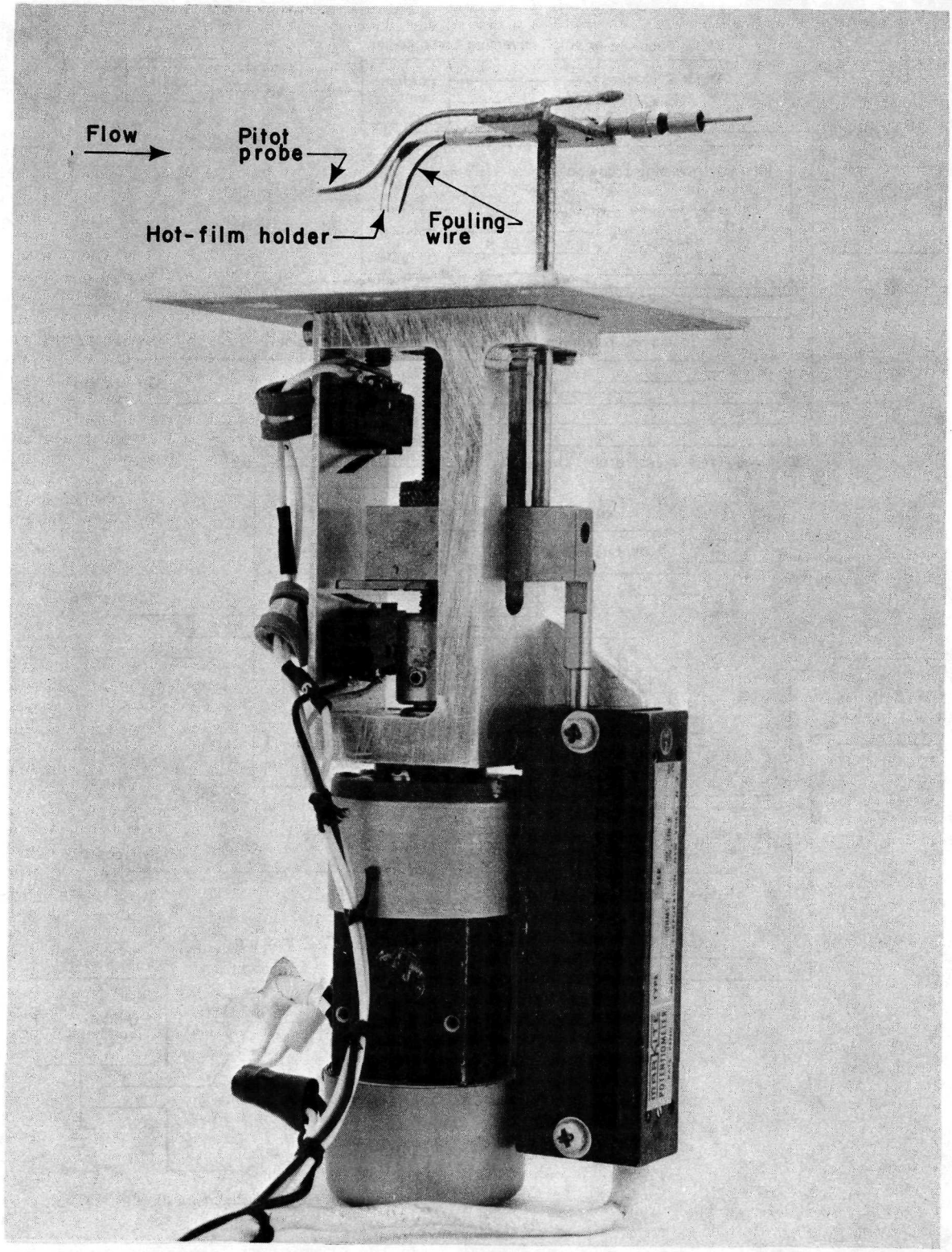

Figure 4. Internal, traversing probe holder with total-pressure and hot-film probes.

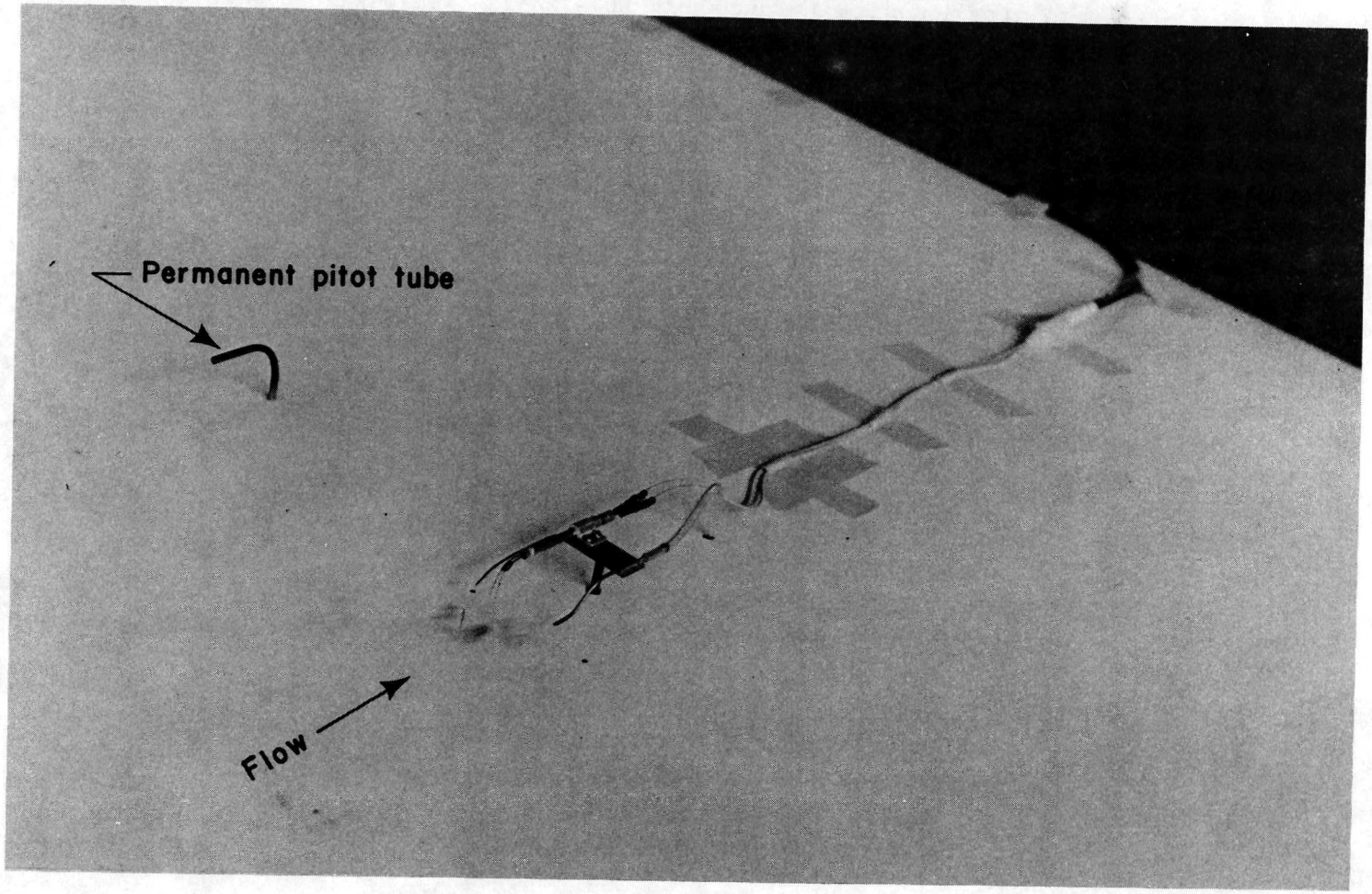

Figure 5. Internal, traversing probe holder, with total-pressure and hot-film probes, mounted on glove.

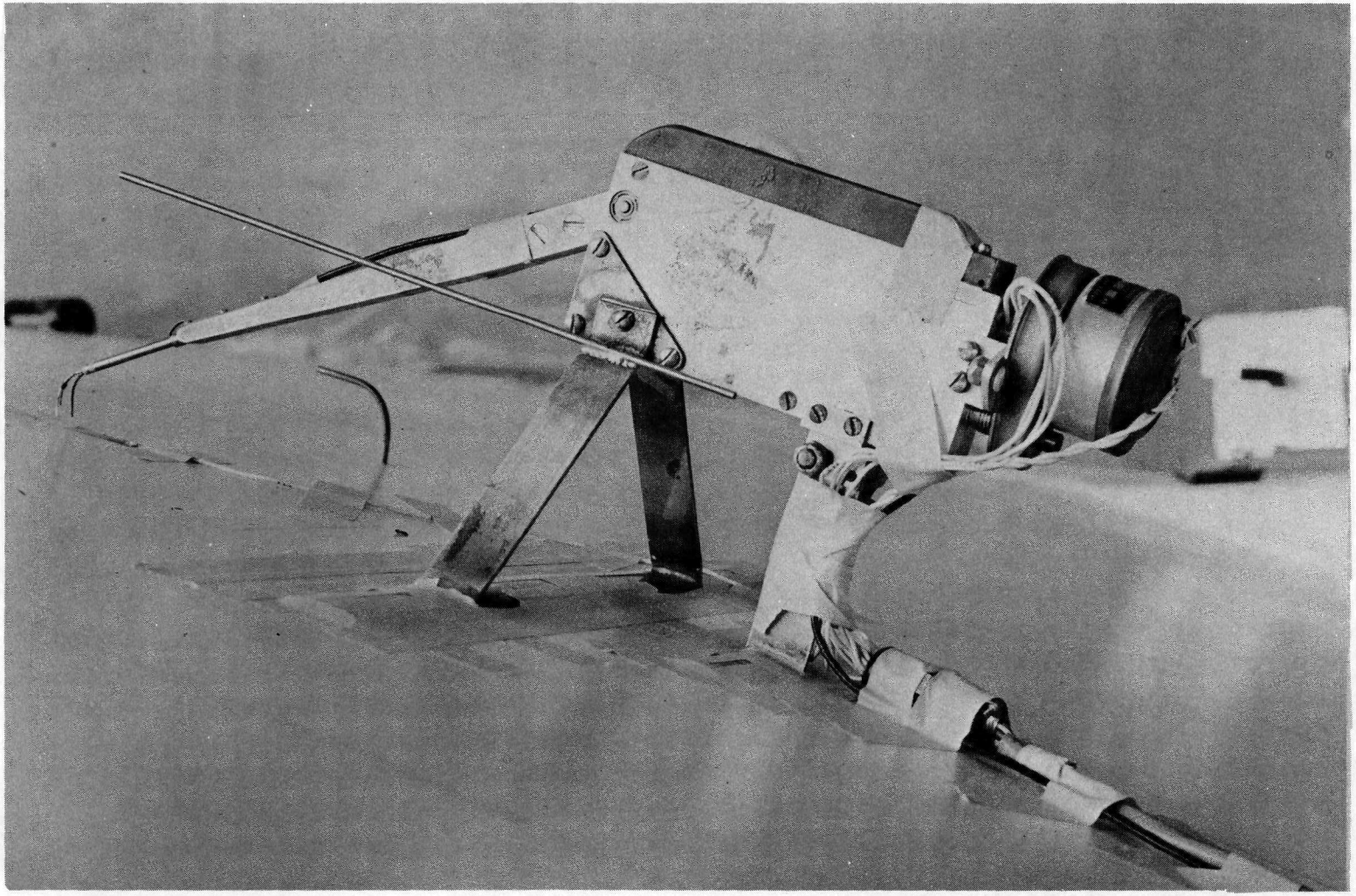

Figure 6. External, traversing probe holder with hot-film probe.

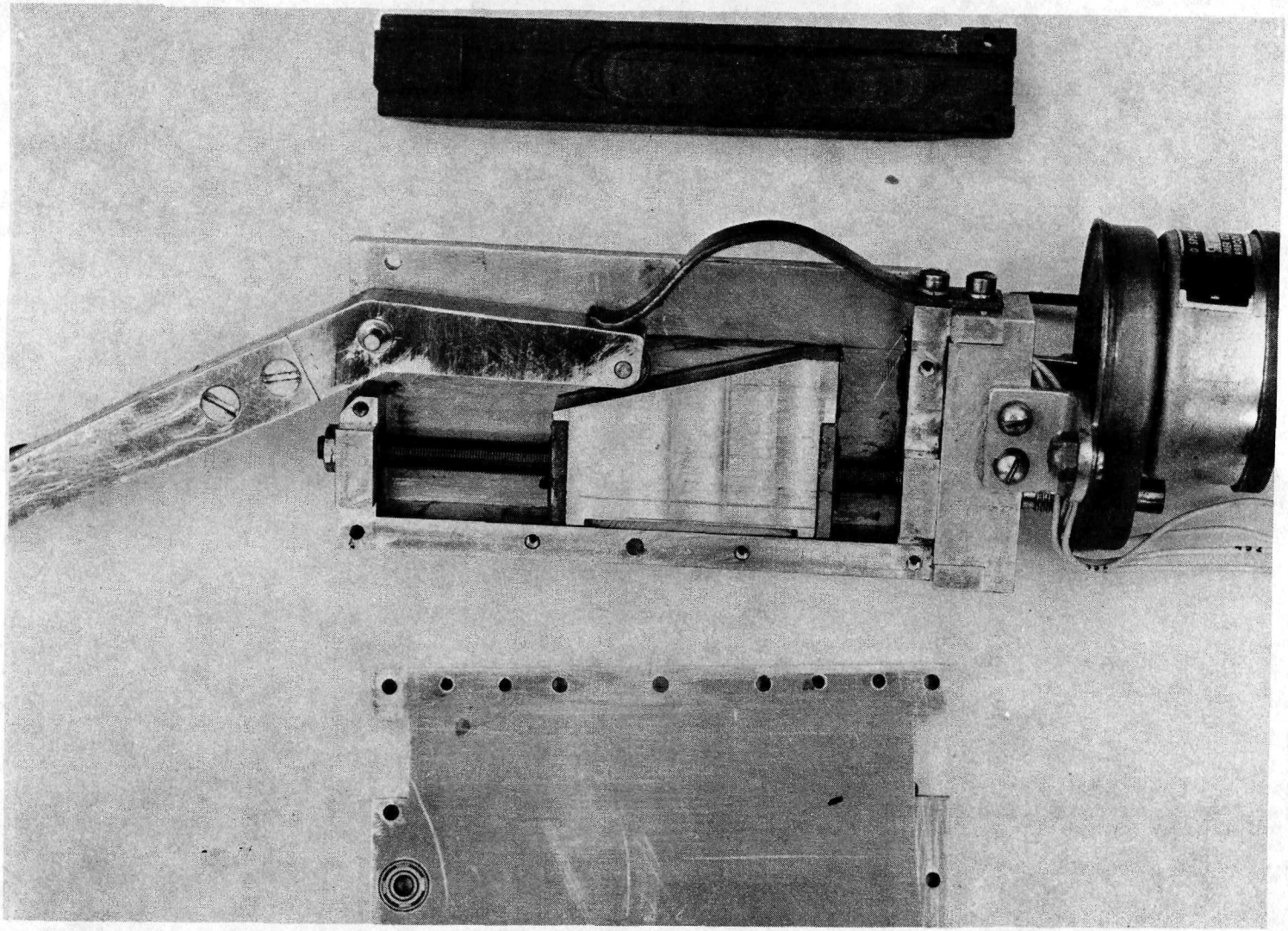

Figure 7. Interior view of external, traversing probe holder.

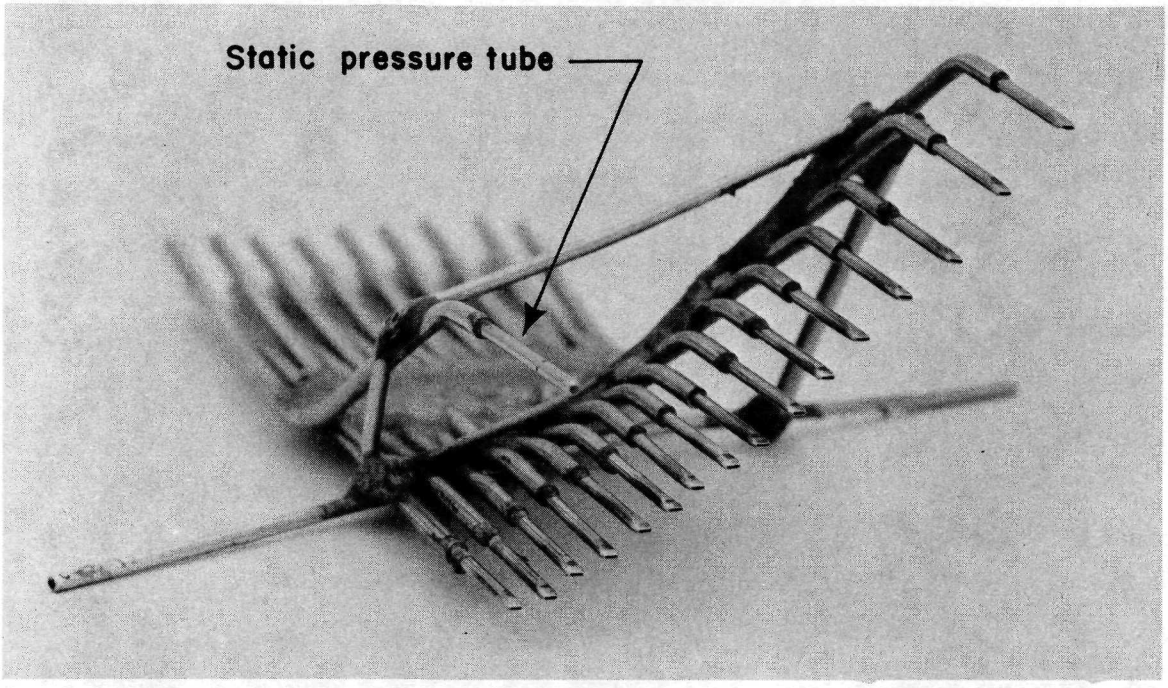

Figure 8. Curved, boundary-layer rake.

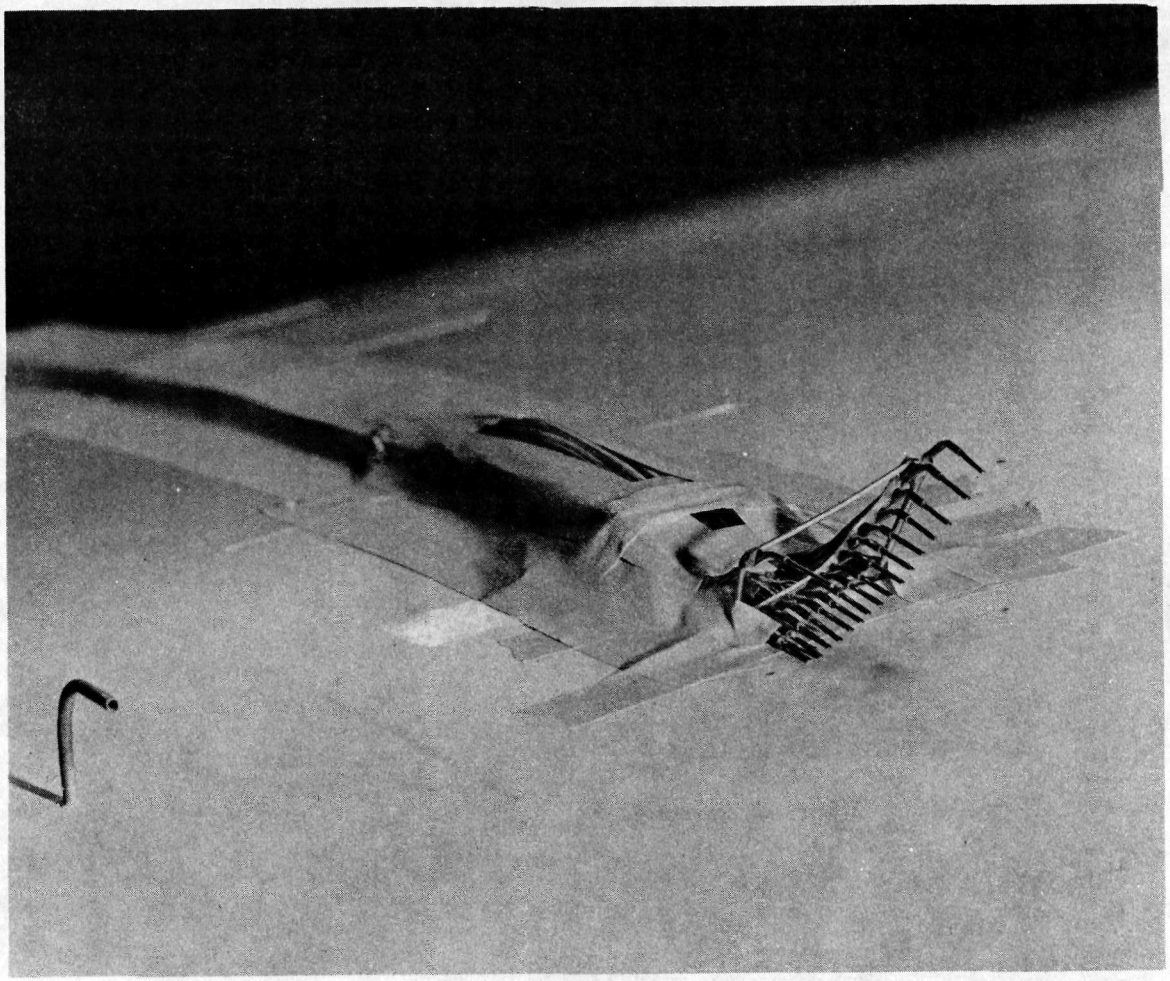

Figure 9. Curved, boundary-layer rake mounted on glove.

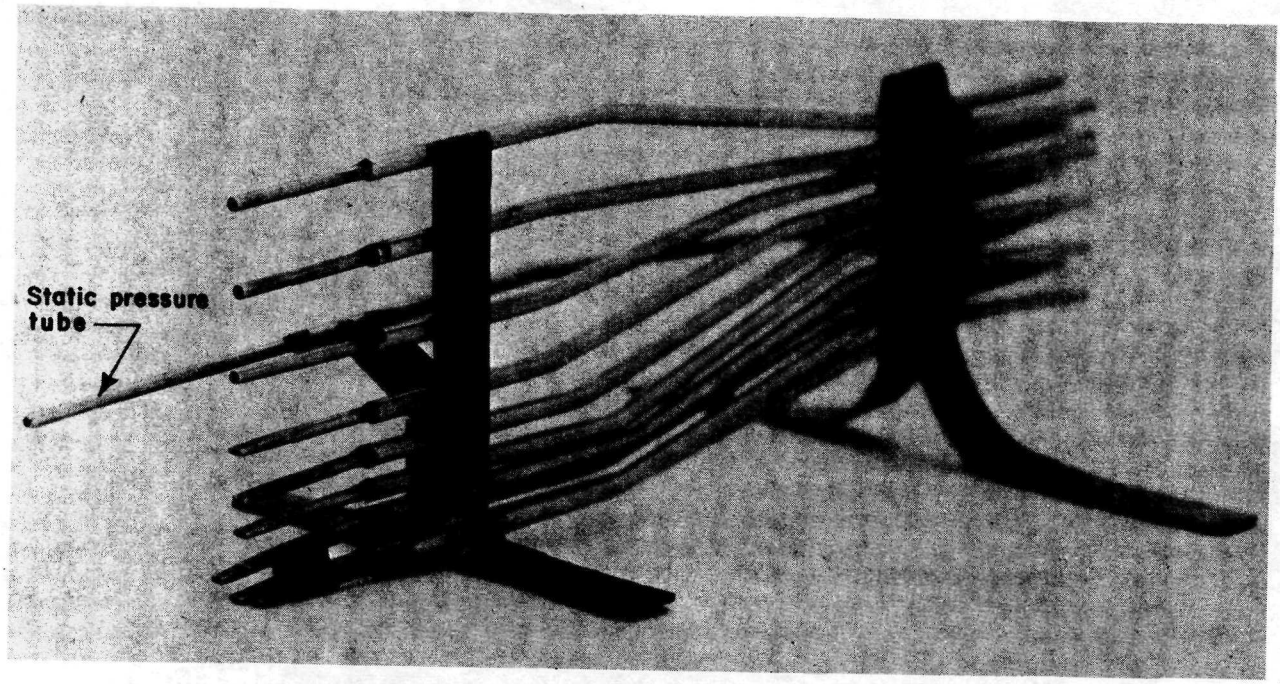

Figure 10. Straight, boundary-layer rake.

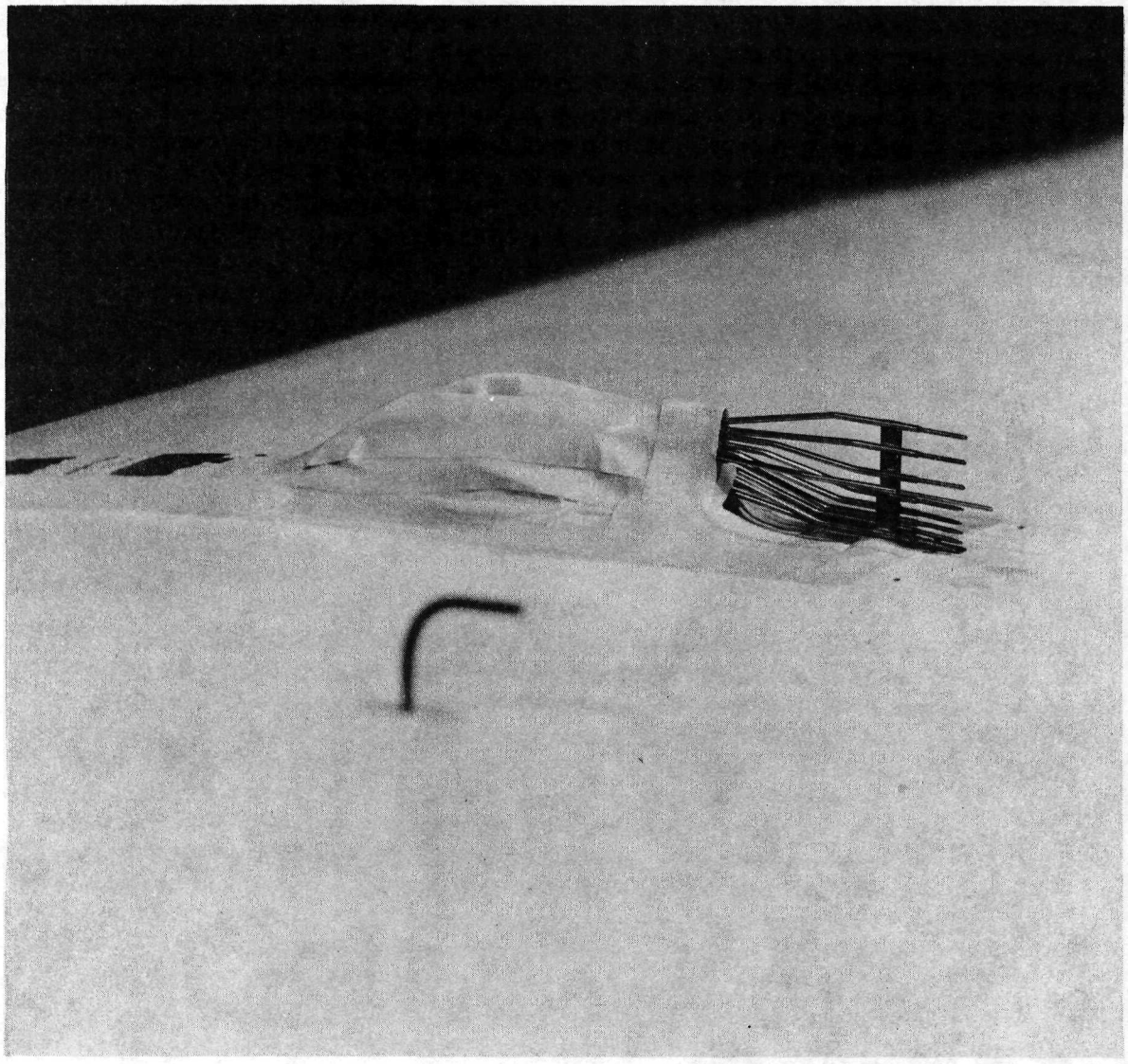

Figure 11. Straight, boundary-layer rake mounted on glove.

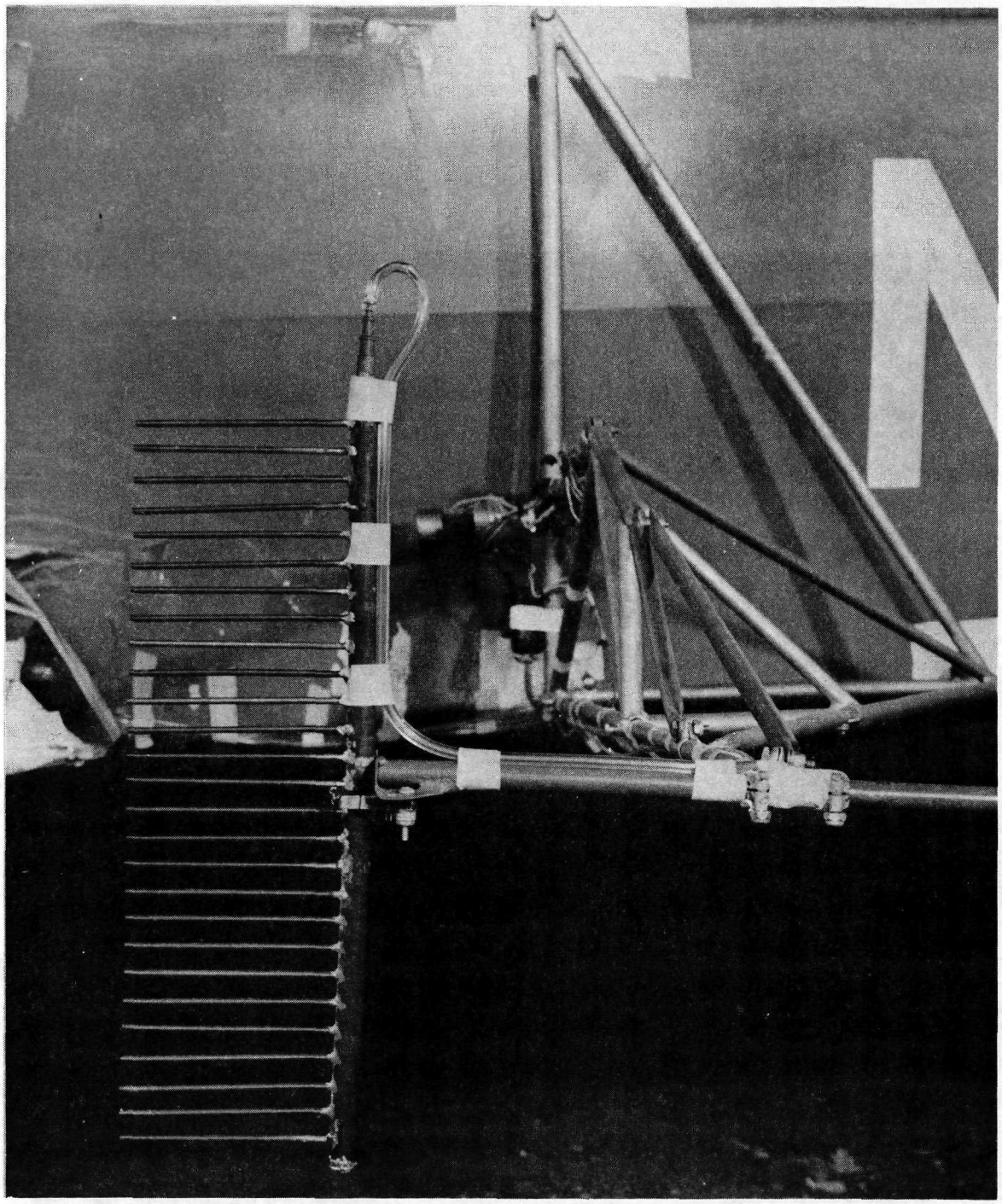

Figure 12. Installation of the integrating wake rake.

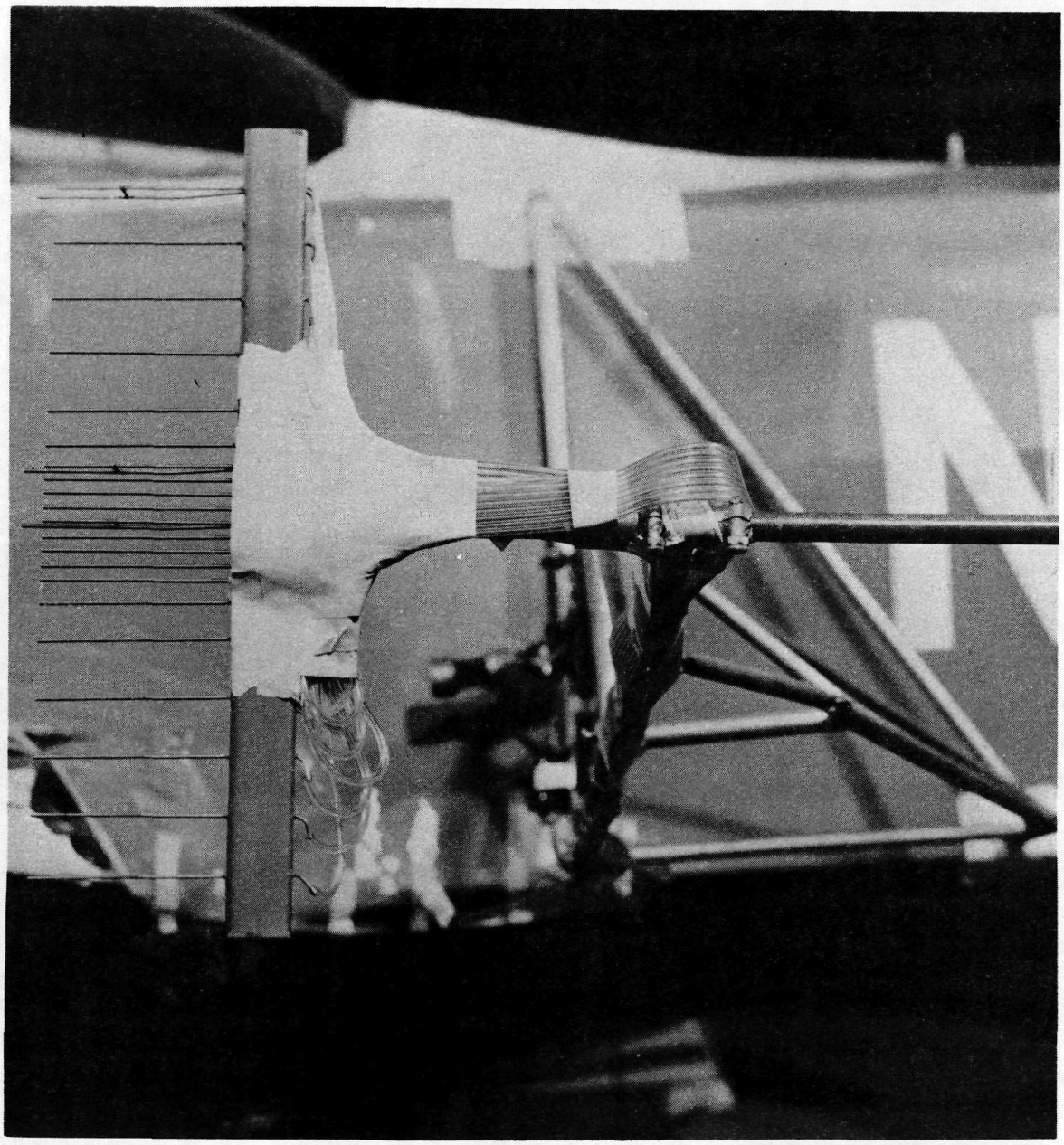

Figure 13. Installation of the wake rake.

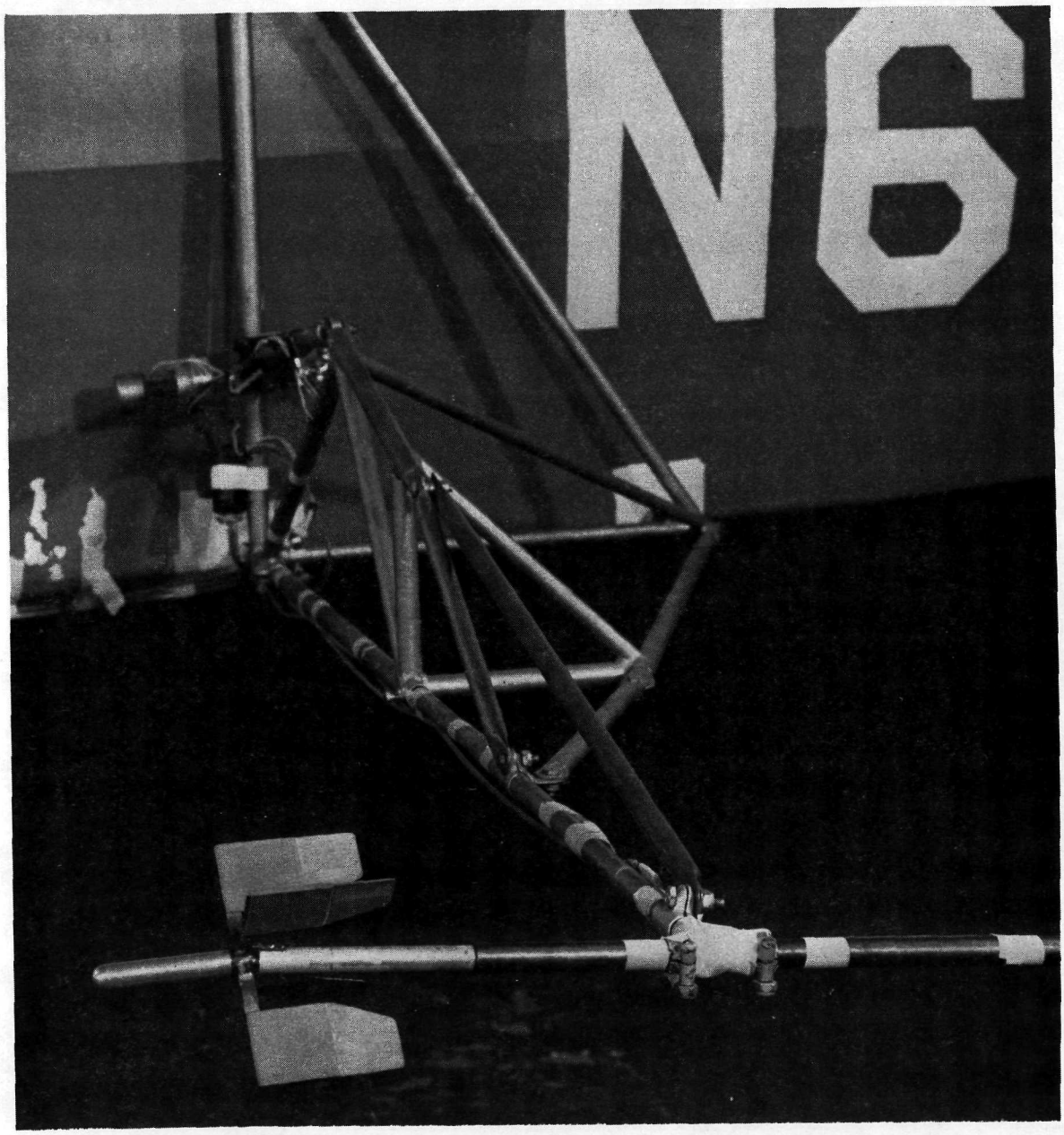

Figure 14. Installation of the self-aligning, traversing, wake probe.

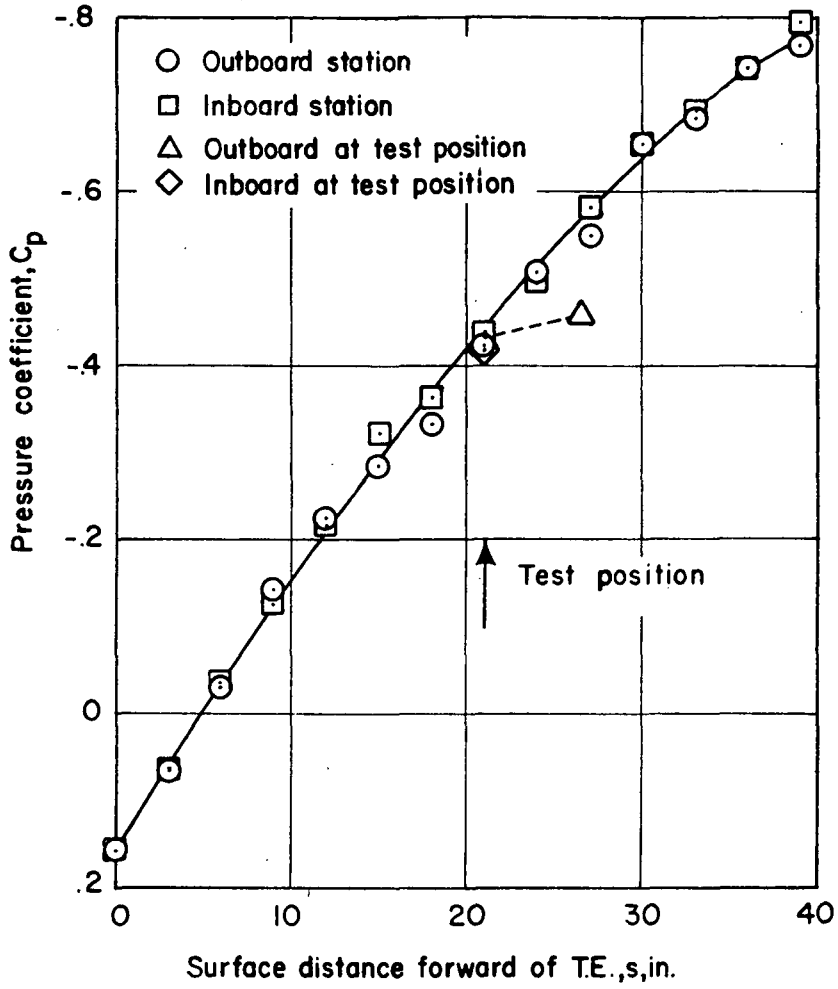

Figure 15. Chordwise, pressure distribution for an aircraft equivalent airspeed of 91.4 miles per hour.

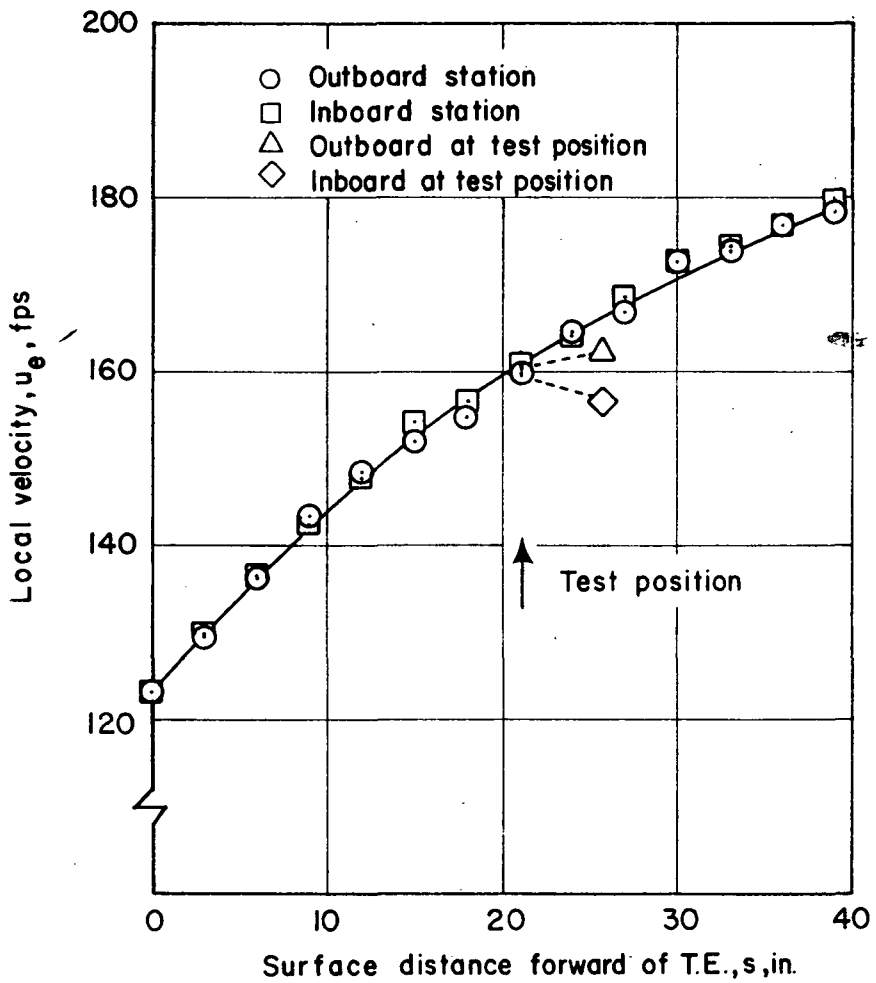

Figure 16. Chordwise, local-velocity distribution for an aircraft equivalent airspeed of 91.4 miles per hour.

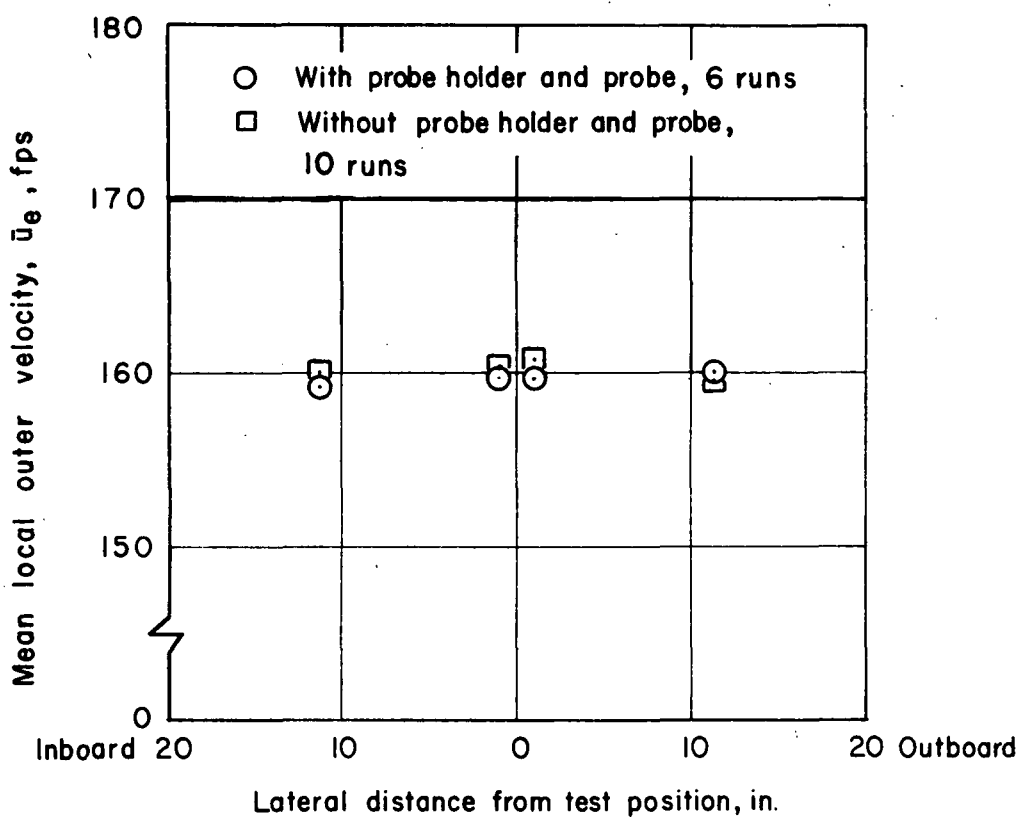

Figure 17. Spanwise, velocity distribution with the internal, traversing probe holder and total-pressure probe.

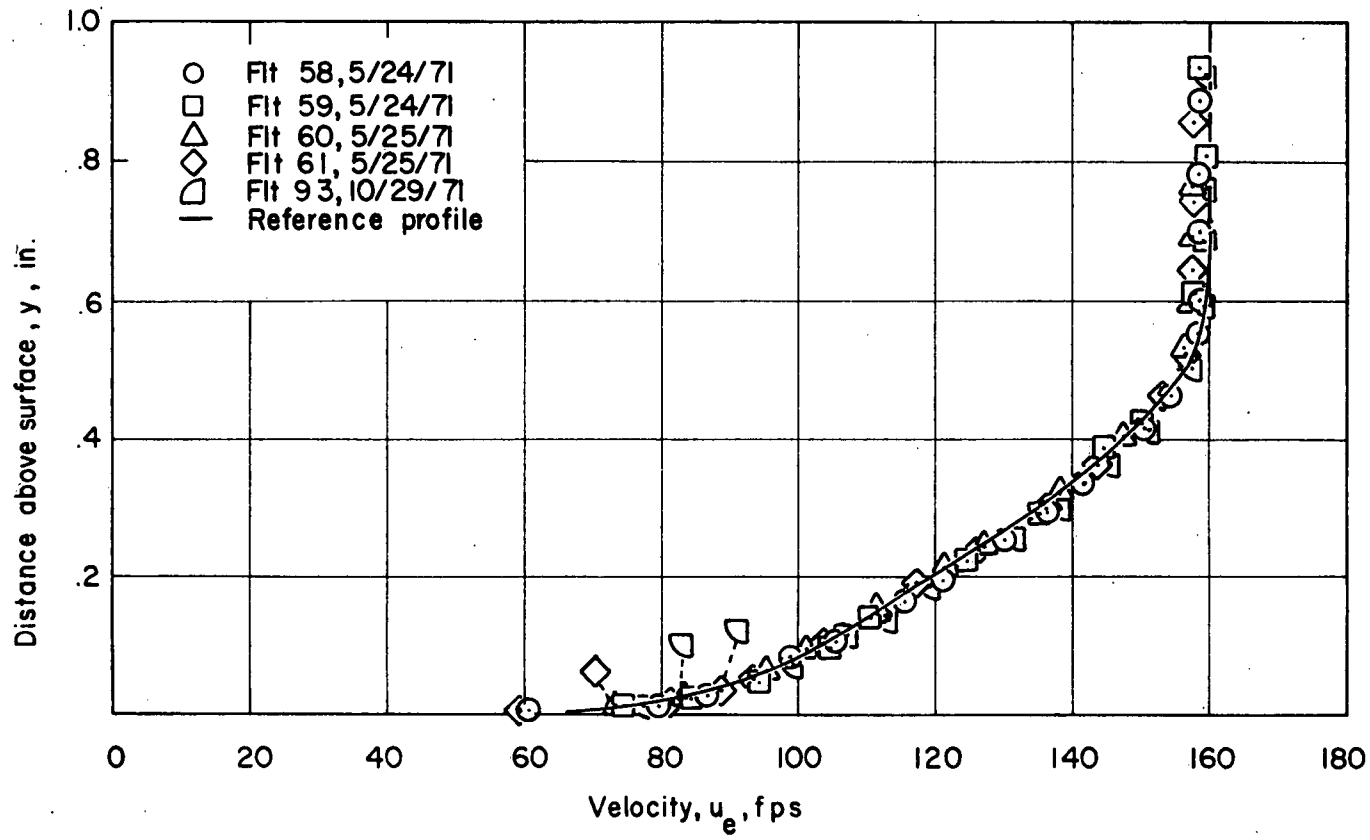

Figure 18. Boundary-layer velocity profile from the internal, traversing probe holder and total-pressure probe.

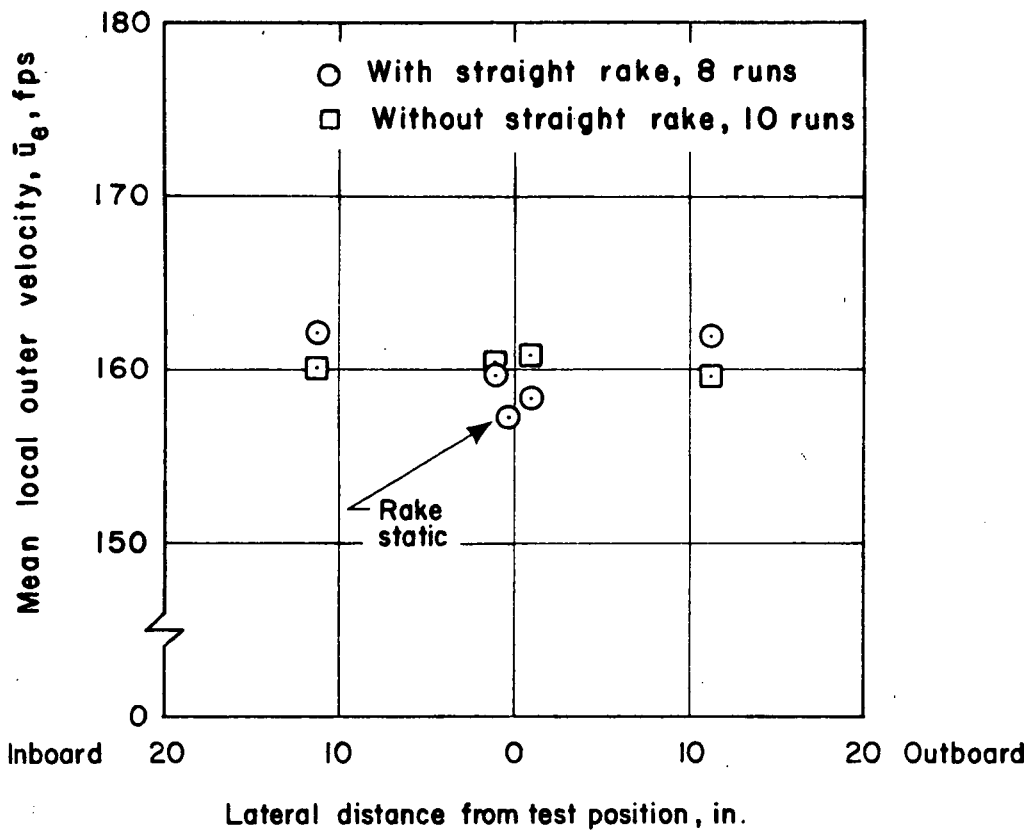

Figure 19. Spanwise, velocity distribution with the straight, boundary-layer rake.

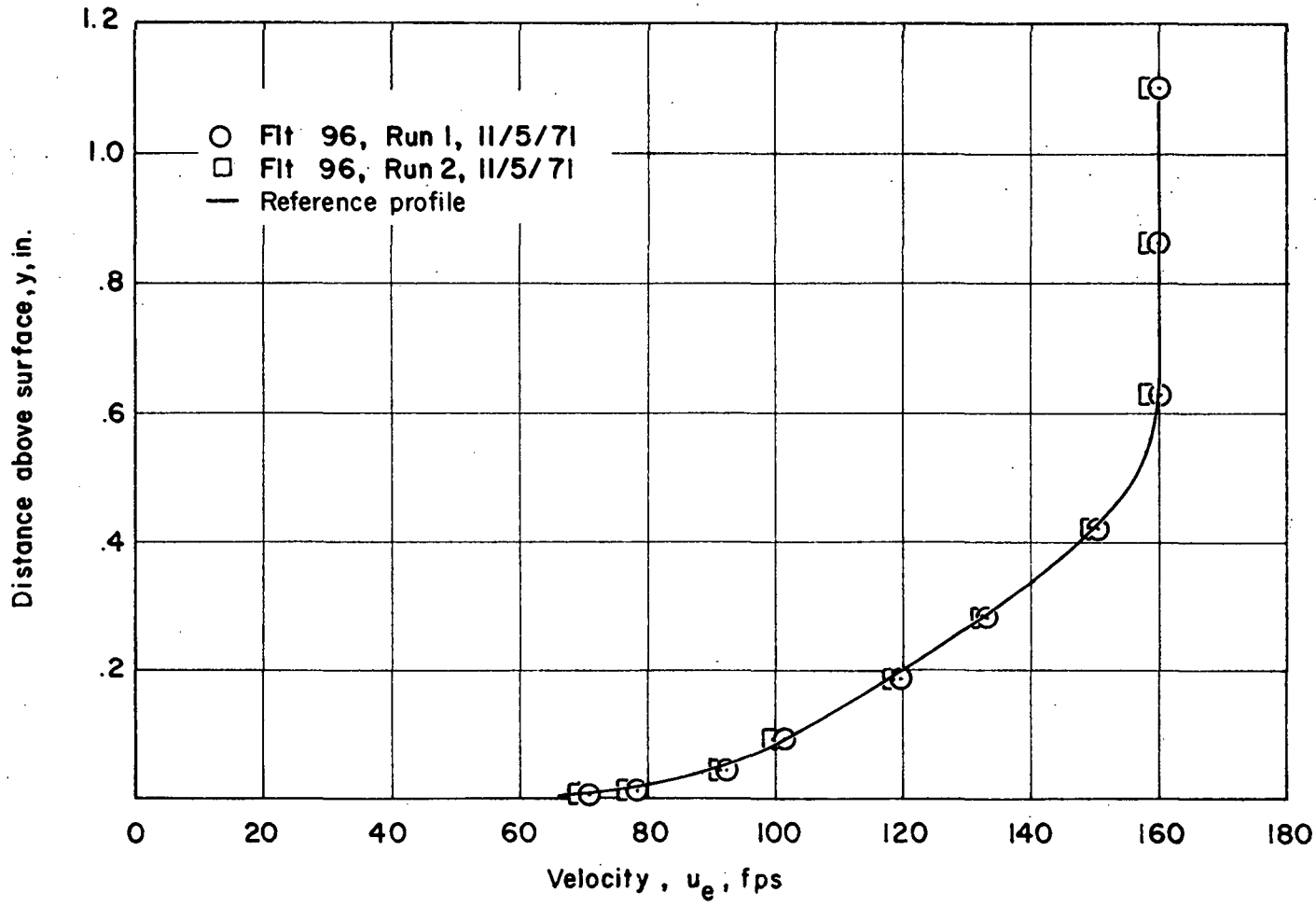

Figure 20. Boundary-layer velocity profile from the straight, boundary-layer rake.

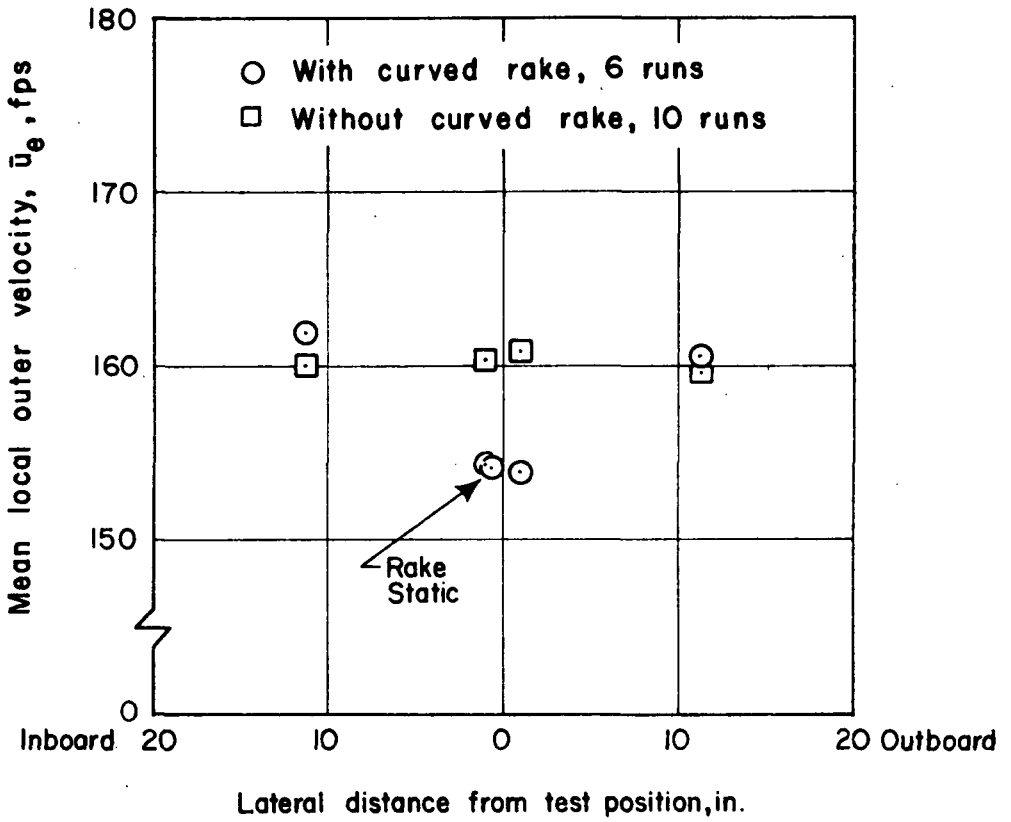

Figure 21. Spanwise velocity distribution with the curved, boundary-layer rake.

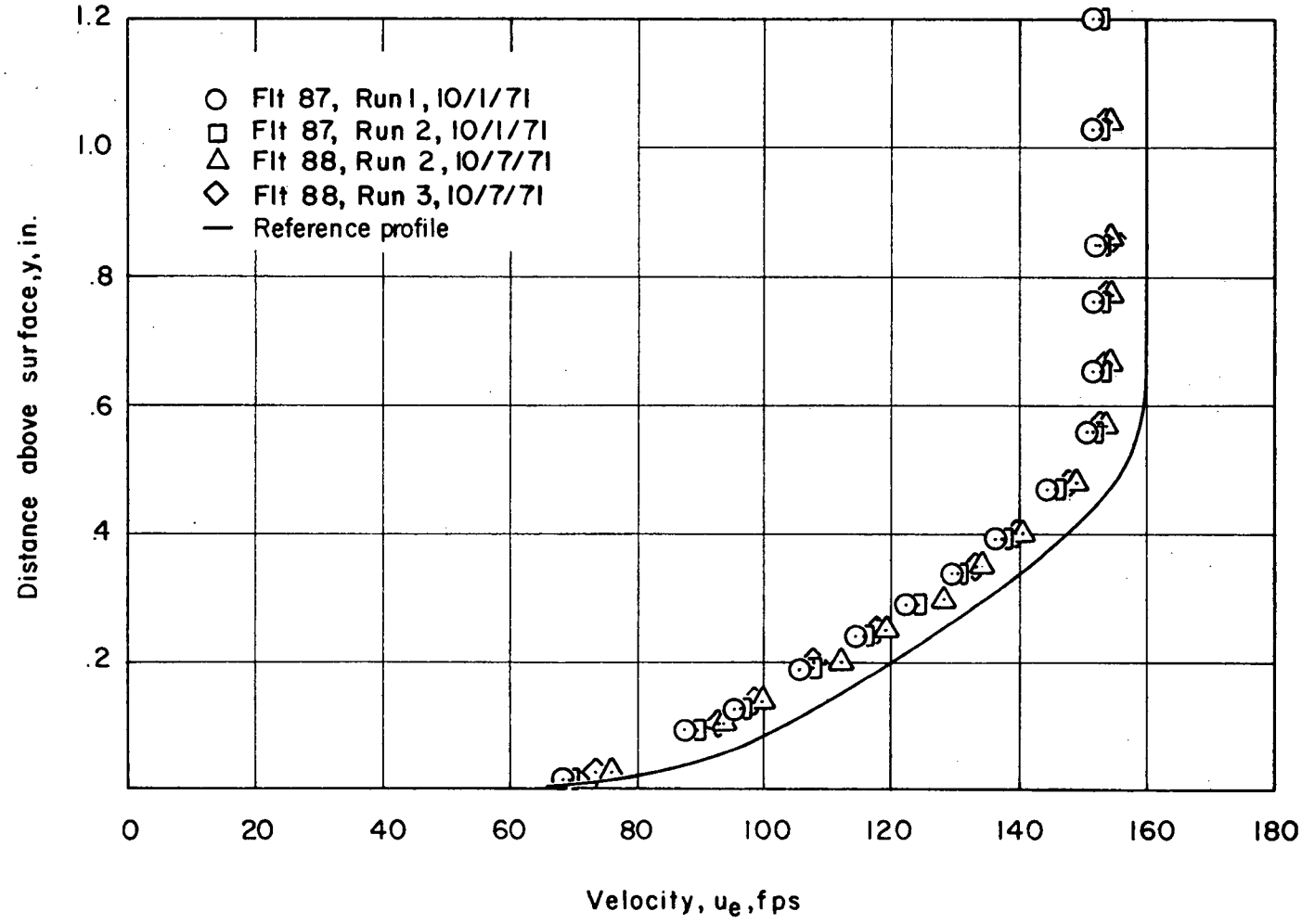

Figure 22. Boundary-layer velocity profile from the curved, boundary-layer rake.

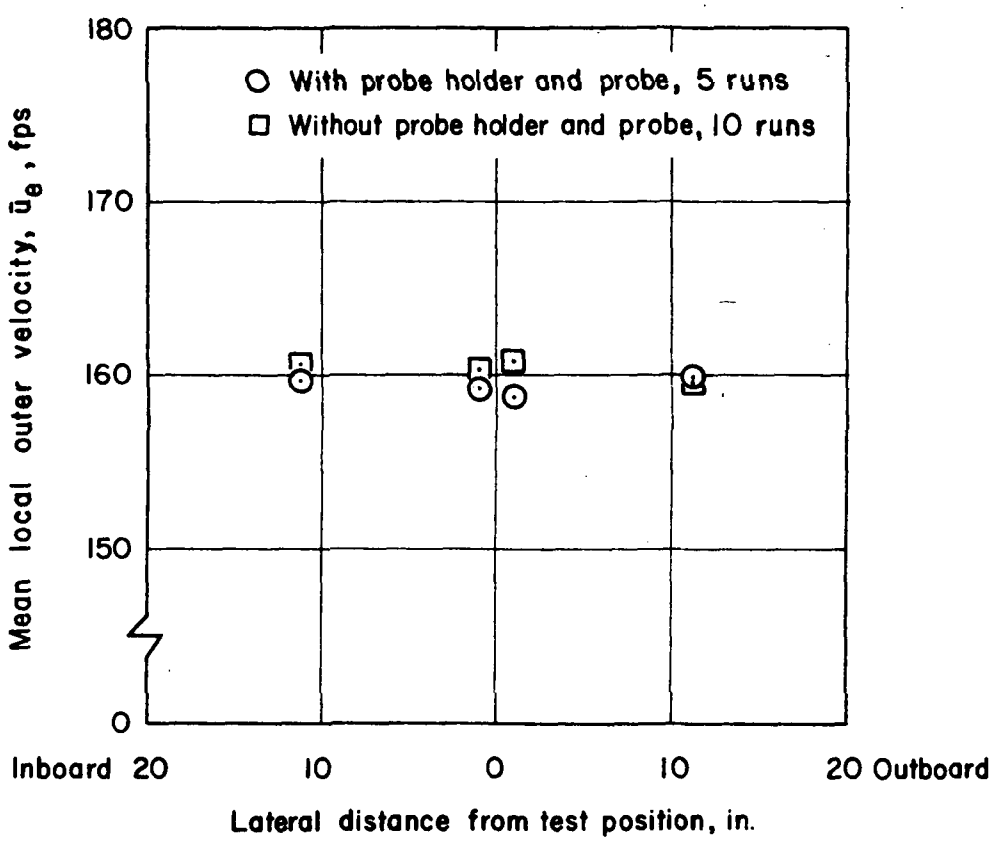

Figure 23. Spanwise, velocity distribution with the internal, traversing probe holder, total-pressure probe, and hot-film probe.

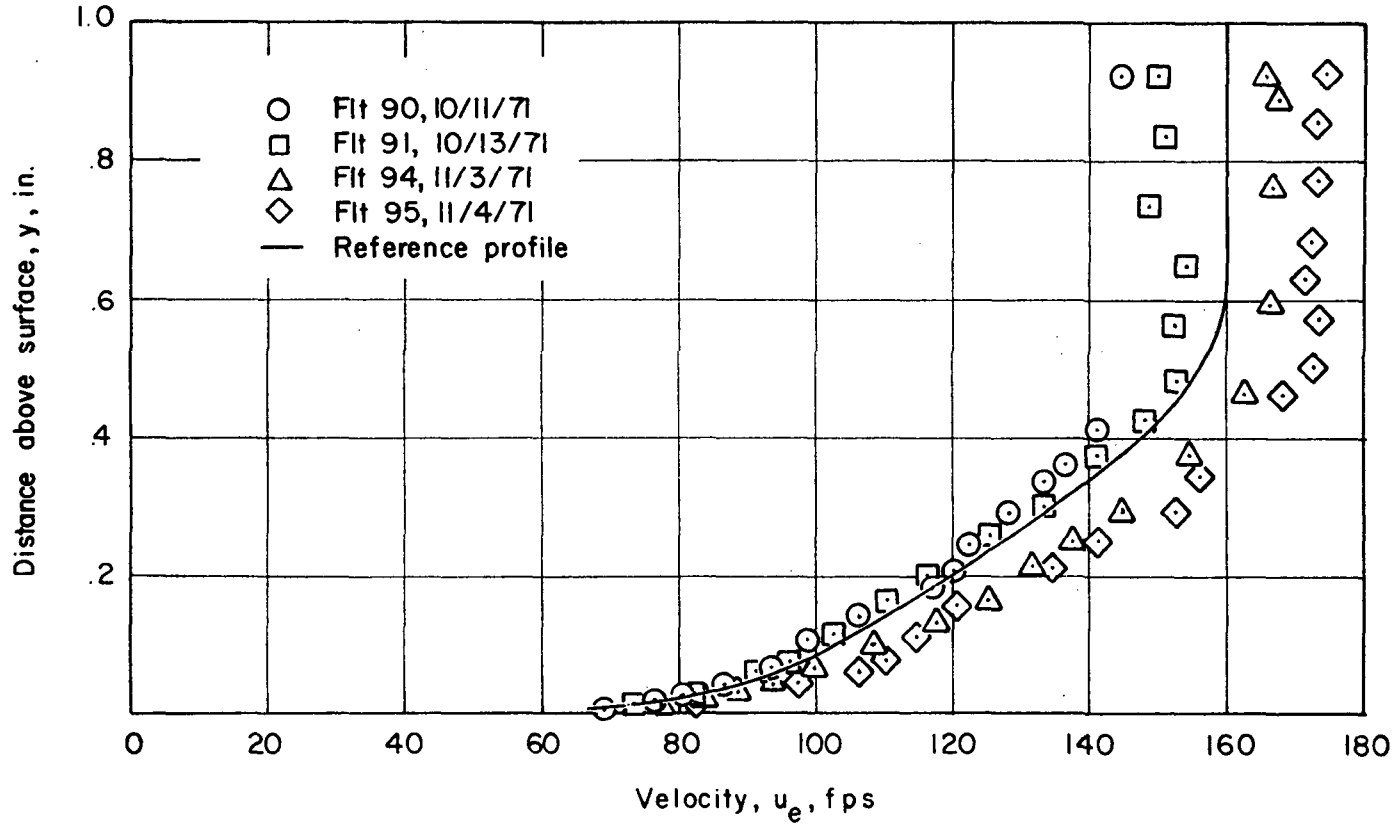

Figure 24. Boundary-layer velocity profile from the internal, traversing probe holder, and hot-film probe. Sensor 1-Y.

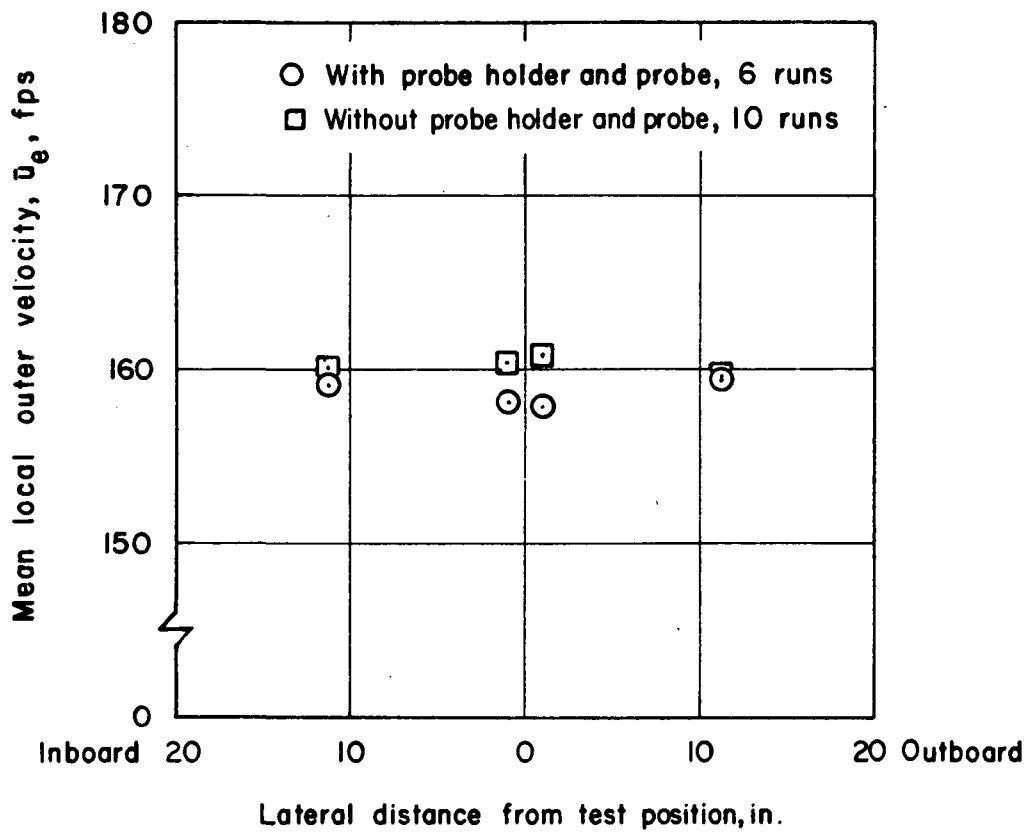

Figure 25. Spanwise, velocity distribution with the external, traversing probe holder and hot-film probe.

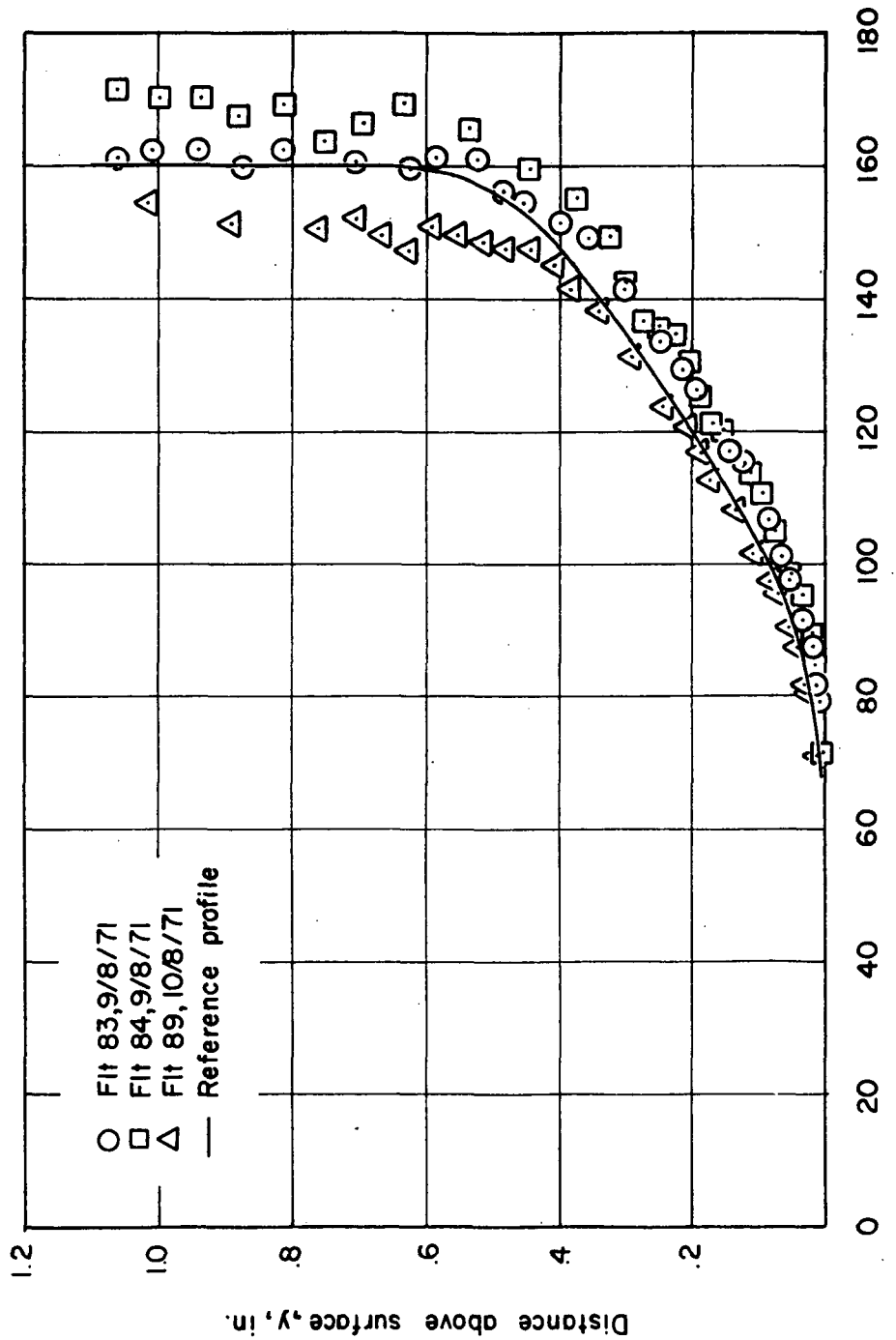

Figure 26. Boundary-layer velocity profile from the external, traversing probe holder and hot-film probe. Sensor 1-Y.

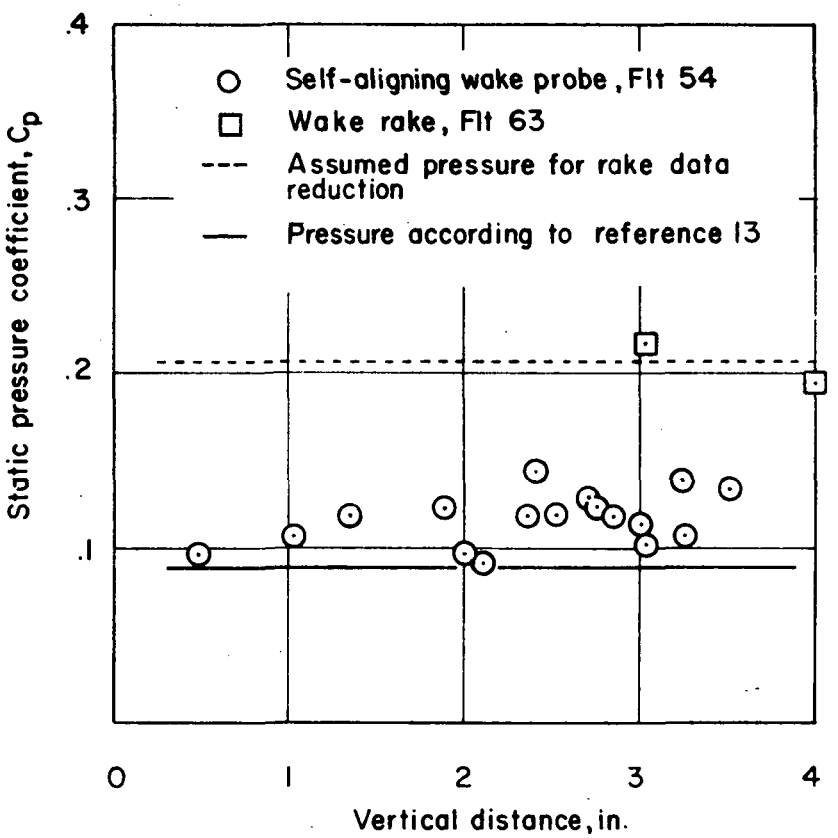

Figure 27. Wake static-pressure measurements.

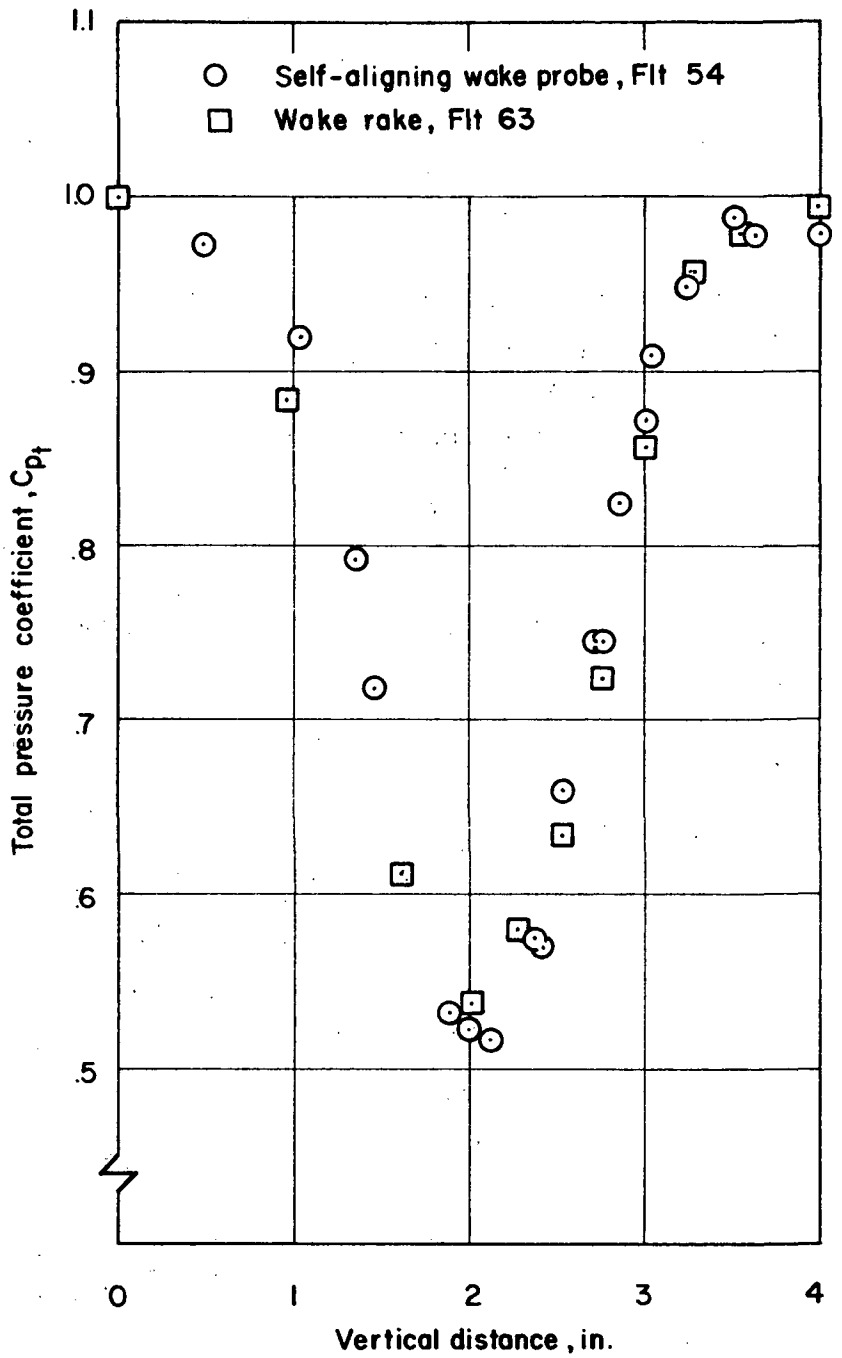

Figure 28. Wake total-pressure measurements.

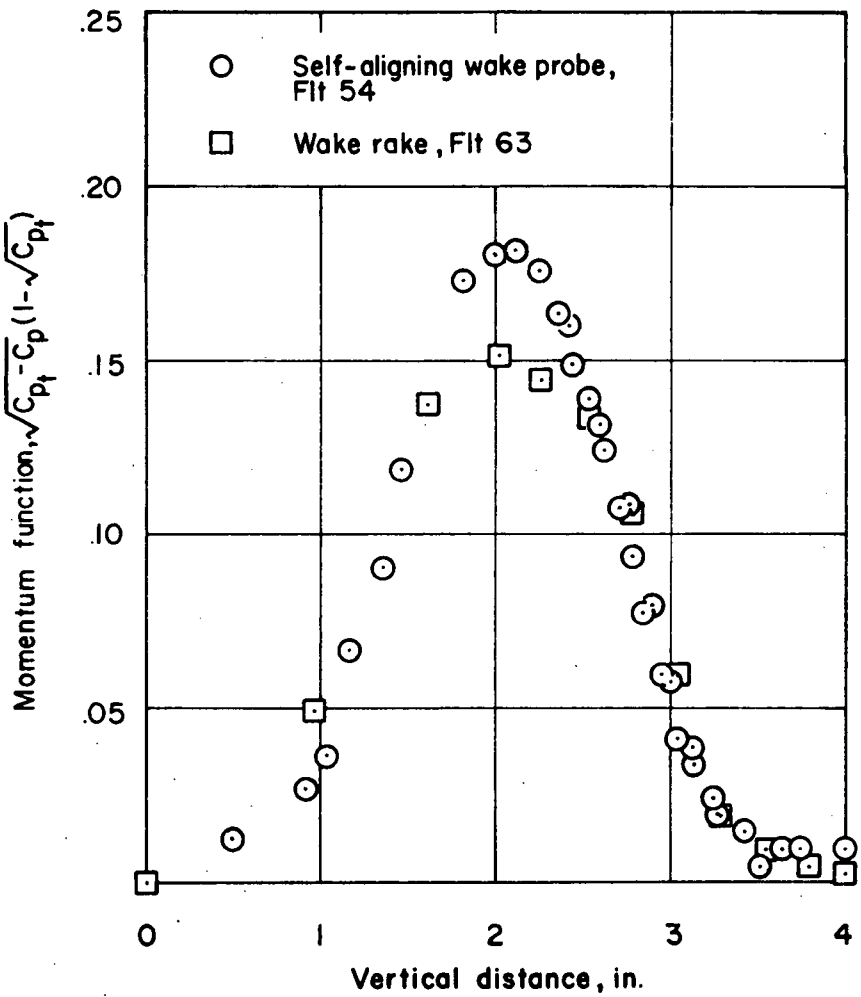

Figure 29. Wake momentum function distribution. Jones' method.

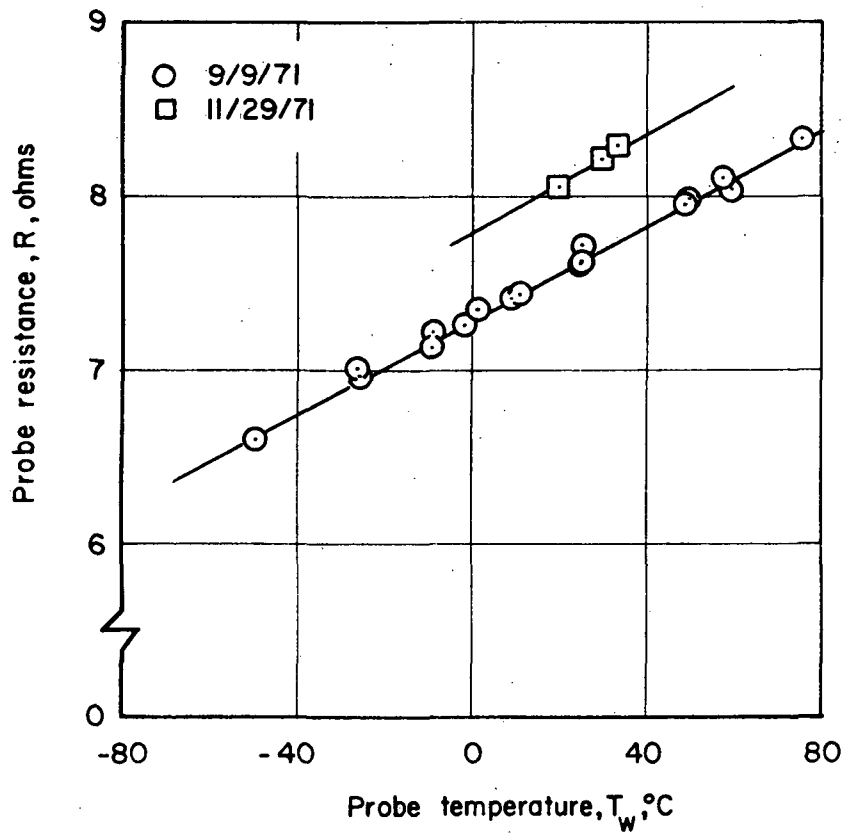

Figure 30. Variation in hot-film probe resistance with probe temperature. Sensor 1-Y.

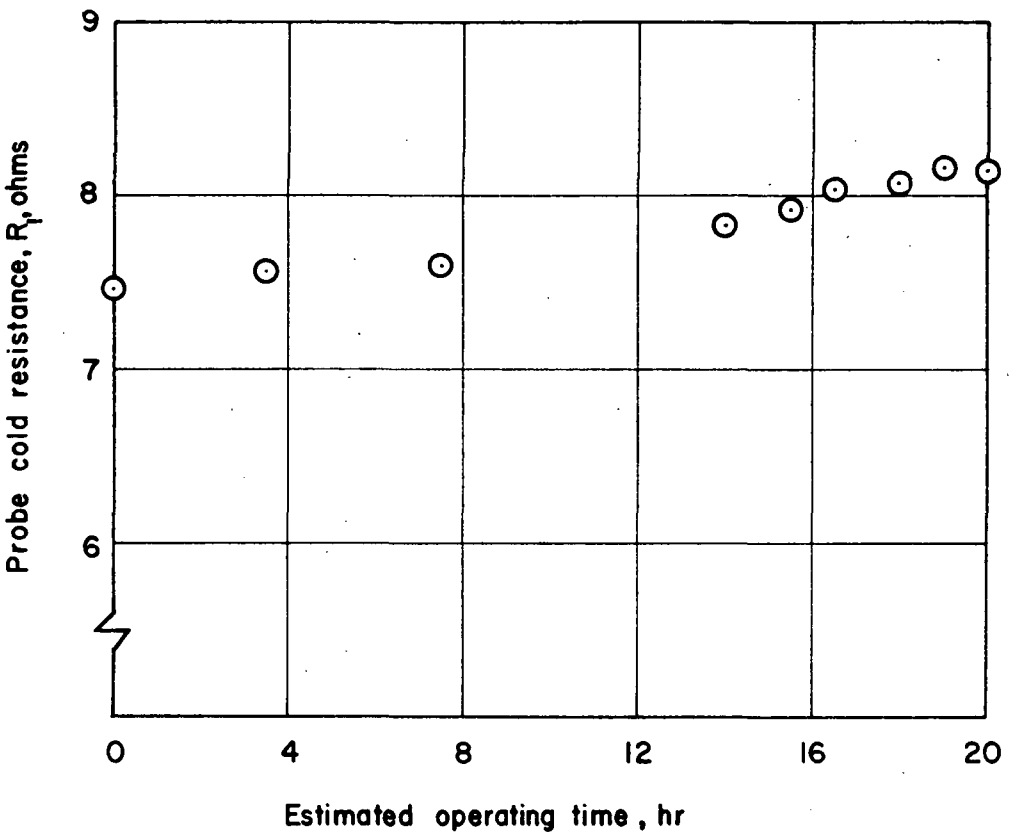

Figure 31. Variation in hot-film probe cold resistance with estimated operating time. Sensor 1-Y.

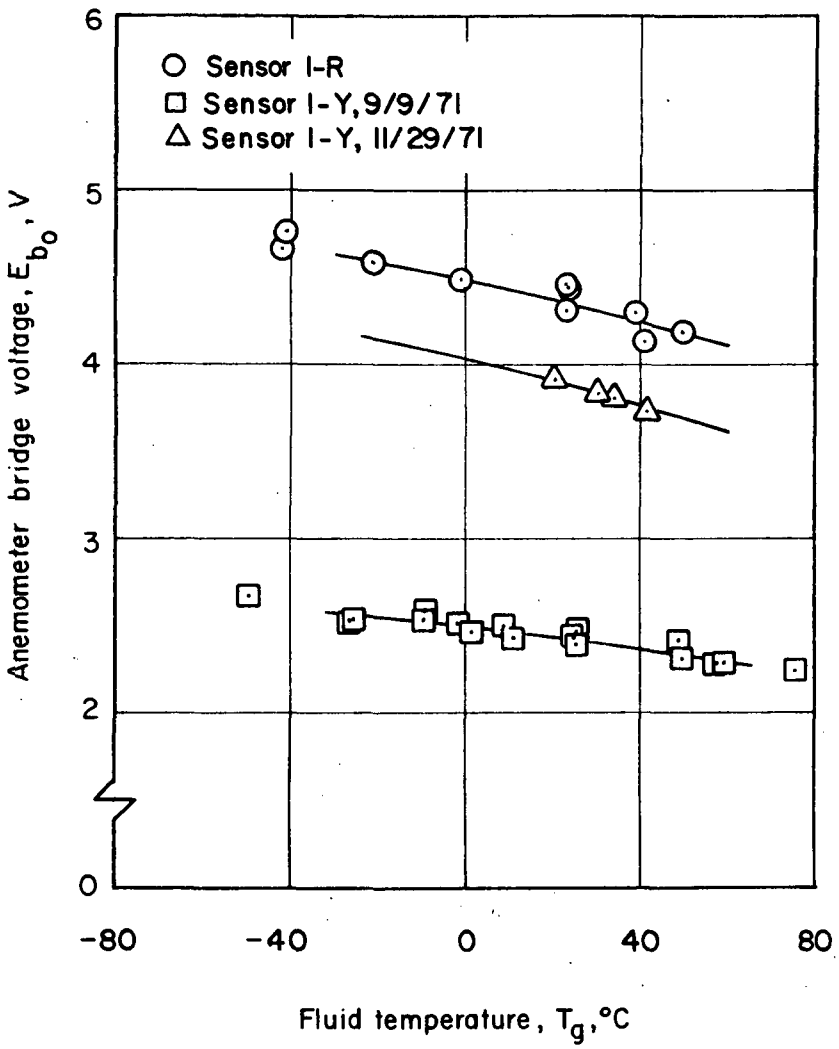

Figure 32. Variation in zero-velocity, anemometer, bridge voltage with fluid temperature.

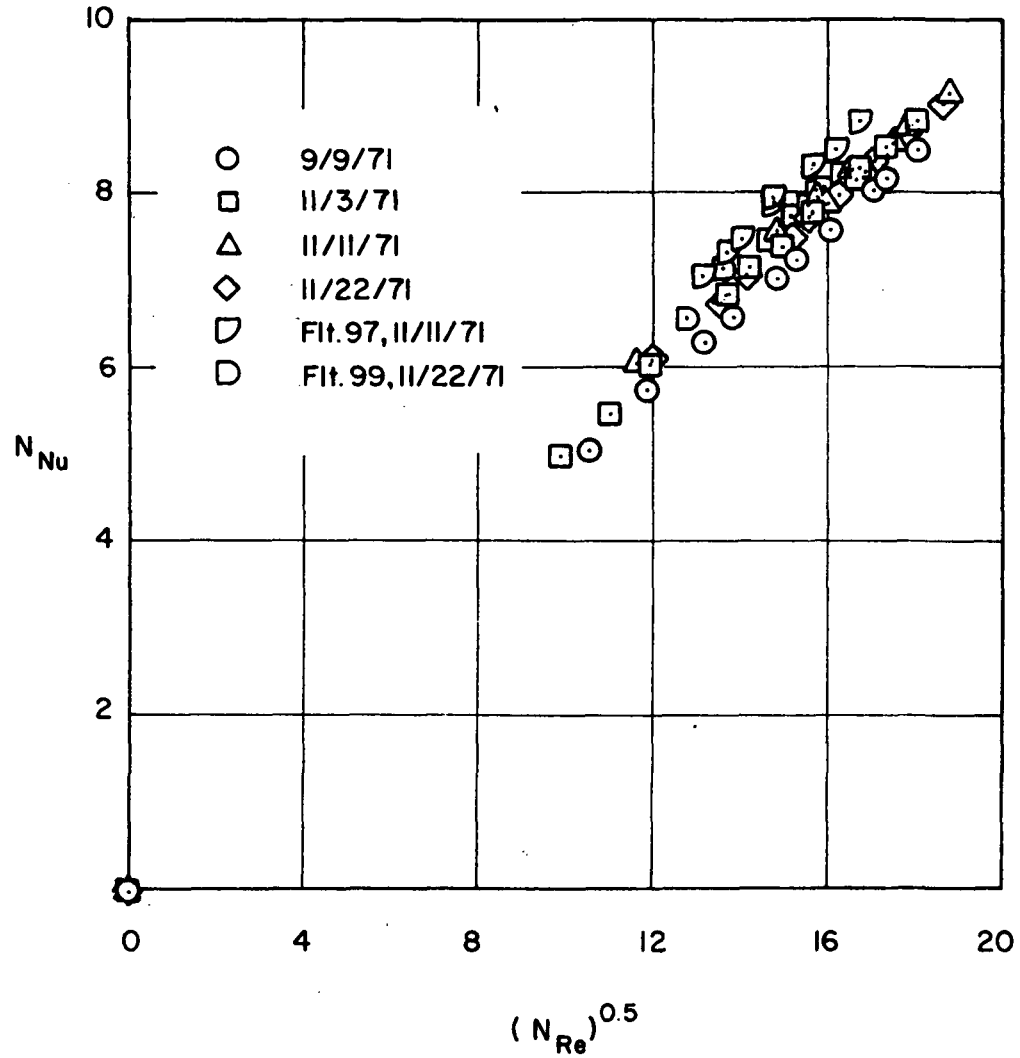

Figure 33. Hot-film probe calibration, N_{Nu} vs. $(N_{Re})^{0.5}$, using film temperature and removing zero-velocity sensor power. Sensor 1-Y.

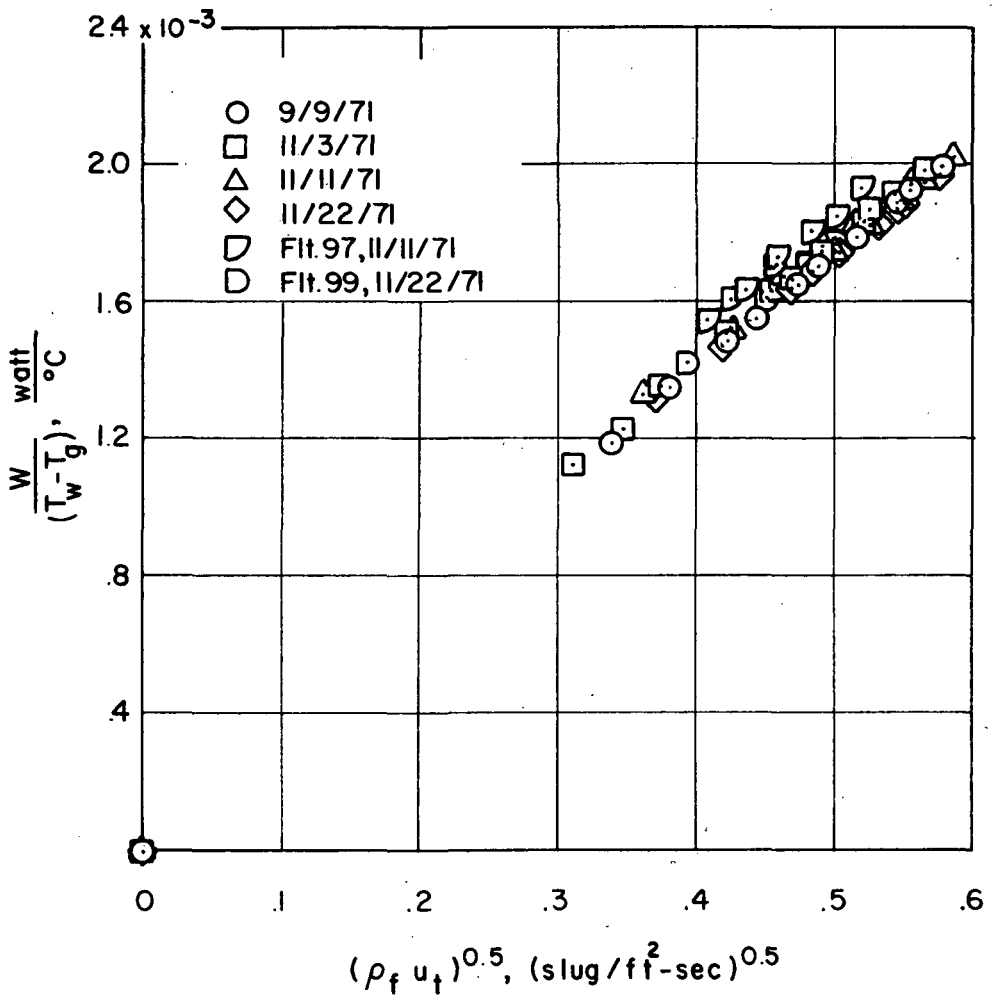

Figure 34. Hot-film probe calibration, $W/(T_w-T_g)$ vs. $(\rho_f u_t)^{0.5}$, using film temperature and removing zero-velocity sensor power. Sensor 1-Y.

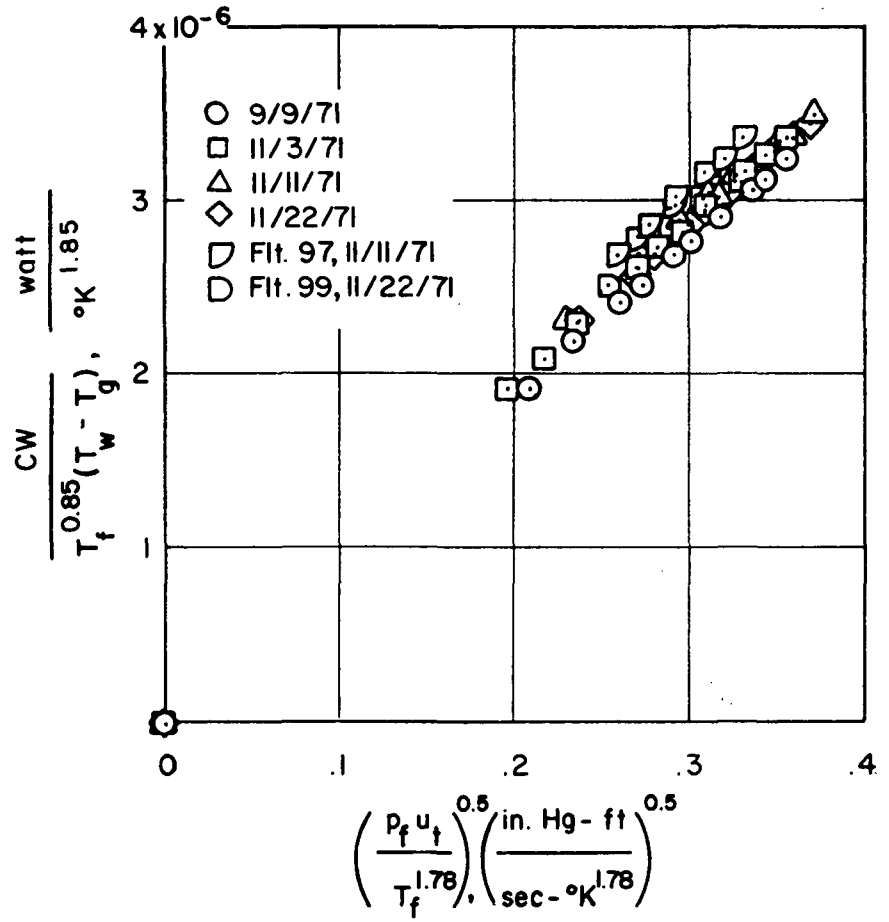

Figure 35. Hot-film probe calibration, $CW/T_f^{0.85}(T_w-T_g)$ vs. $\left[\rho_f u_t/T_f^{1.78}\right]^{0.5}$, using film temperature and removing zero-velocity sensor power. Sensor 1-Y.